Remote Sensing Applications: Society and Environment 40 (2025) 101722

Contents lists available at ScienceDirect

Remote Sensing Applications: Society and Environment

journal homepage: www.elsevier.com/locate/rsase

Development of a litho-structural map for the Upper Mereb area, Eritrea, using multi-source remote sensing data and machine learning models

Kabral Mogos Asghede [a,b,*], Abazar M.A. Daoud [c,d], Musaab A.A. Mohammed [a,e], Woldegabriel Genzebu [f], Kefela Beyene Kiflay [f], Péter Pecsmány [a], János Vágó [a]

[a] *Faculty of Earth and Environmental Sciences and Engineering, University of Miskolc, 3515, Miskolc, Hungary*
[b] *Department of Civil Engineering, College of Engineering and Technology, Mai-Nefhi, Eritrea*
[c] *Department of Mineralogy and Geology, University of Debrecen, Egyetem Tér 1, 4032, Hungary*
[d] *Faculty of Earth Sciences, Red Sea University, PortSudan, Sudan*
[e] *College of Petroleum Geology and Minerals, University of Bahri, Khartoum, Sudan*
[f] *Department of Earth Science, Mai-Nefhi College of Science, Eritrea*

ARTICLE INFO

Keywords:
Machine learning
Remote sensing
Gravity
Structural analysis
Geological mapping

ABSTRACT

The Upper Mereb catchment area, located on the Southern zone of Eritrea, is a geologically complex region within the Arabian-Nubian Shield (ANS). The area's intricate litho-structural framework presents significant challenges for mineral exploration and groundwater investigations. Traditional geological mapping techniques often struggle to capture the fine-scale structural details necessary for resource assessments in such complex terrains. This study introduces a novel, high-resolution litho-structural mapping approach, integrating Landsat 9 (L9) multispectral data and gravity data with advanced machine learning algorithms, specifically Artificial Neural Networks (ANN) and Support Vector Machines (SVM). The classification results indicate that ANN outperforms SVM, achieving an accuracy exceeding 79 %, demonstrating the effectiveness of machine learning in distinguishing lithological units. Furthermore, detailed field investigations validate the accuracy of the litho-structural map, showing strong correlations with ground-truth data. A key component of this study is the structural analysis of lineament orientations, which provides critical insights into the tectonic evolution of the region. The Pan-African orogeny has significantly influenced the structural framework, with dominant NE-SW compressional forces creations the fracture patterns. The identified lineaments fall into three primary sets: NW-SE extensional fractures, indicative of crustal stretching; NE-SW release fractures, reflecting zones of stress relaxation; and N-S shear fractures, formed under oblique stress conditions. These structural features highlight the region's complex deformation history and provide essential information for understanding subsurface fluid flow and resource potential. This study represents the first comprehensive application of an integrated remote sensing and geophysical machine learning approach to geological mapping in the Upper Mereb area. The results emphasize the potential of hybrid remote sensing and geophysical data fusion for enhancing structural interpretations, offering a powerful tool for mineral exploration, groundwater assessments, and tectonic studies in the Arabian-Nubian Shield.

---

[*] Corresponding author. Faculty of Earth and Environmental Sciences and Engineering, University of Miskolc, 3515, Miskolc, Hungary.
E-mail address: kabralmogos@gmail.com (K.M. Asghede).

https://doi.org/10.1016/j.rsase.2025.101722
Received 6 May 2025; Received in revised form 24 August 2025; Accepted 5 September 2025
Available online 12 September 2025
2352-9385/© 2025 The Authors. Published by Elsevier B.V. This is an open access article under the CC BY license (http://creativecommons.org/licenses/by/4.0/).

1. Introduction

The Upper Mereb area in Eritrea represents a geologically complex region characterized by distinct lithological units and structural features. Situated within the Mereb-Gash River Basin (Measho et al., 2020), this region plays a significant role in understanding the broader evolution of the Arabian-Nubian Shield (ANS) and its implications for regional geological processes (Drury et al., 2001; Drury and Berhe, 1993; Drury and De Souza Filho, 1998; Johnson et al., 2013; Stern et al., 2004). The basement rocks exhibit variable degrees of metamorphism and deformation, with localized mafic intrusions to intermediate volcanic formations. Despite its geological significance, the Upper Mereb area lacks detailed lithological mapping, limiting our understanding of its subsurface characteristics and structural framework. Most of the previous studies focus on their groundwater potentiality with a lack of detailed lithological mapping, especially using satellite image platforms such as Landsat 9 (L9) enhanced using the panchromatic band (B8) to a spatial resolution of 15 m. Traditional geological mapping methods realize confrontations due to extensive weathering, vegetation cover, and the complexity of rock units. In this context, integrating remote sensing and geophysical techniques offers a powerful approach to overcoming these limitations.

Gravity data are particularly useful in detecting subsurface structures and density contrasts within the subsurface, allowing for the delineation of lithological boundaries and fault zones. High-density basement rocks can be distinguished from overlying sedimentary sequences, revealing the extent and geometry of concealed structural features (Camacho and Alvarez, 2021; Daoud et al., 2025; Davies et al., 2025; Grauch and Cordell, 1987; Hirt et al., 2013; Kassa, 2024; Melo and Li, 2021; Piegari et al., 2023; Pradhan et al., 2022; Pratama et al., 2023). Meanwhile, remote sensing, mainly through multispectral and hyperspectral imaging, enhances surface mapping by identifying lithological variations, alteration zones, and structural discontinuities that may not be obvious in field surveys. In recent years, machine learning (ML) has developed as a transformative tool in lithological mapping, advancing improved classification accuracy and automation in geological interpretation. Supervised learning algorithms, such as Support Vector Machines (SVM), Random Forest (RF), and Artificial Neural Networks (ANN), have been increasingly applied to classify lithological units based on remotely sensed and geophysical datasets (Abdelkader et al., 2022; Davies et al., 2025; El-Omairi et al., 2025; Harris and Grunsky, 2015; Mahboob et al., 2024; Miller et al., 1995; Zuo and Carranza, 2023). SVM, in particular, is well-suited for lithological classification due to its ability to handle complex, high-dimensional datasets and effectively differentiate between spectrally similar rock units (Zuo and Carranza, 2023).

A previous regional-scale remote sensing study conducted by (Solomon and Quiel, 2006) encompassed a broad area, within which our current study area represents a relatively small subset. However, in this study a more detailed and focused analysis was undertaken to explore the lithological complexity at a smaller scale. Using advanced remote sensing techniques and gravity data, we identified previously unrecognized lithological variations within the study area. Several false color composites (FCCs), band ratios (BRs), and Principal Component Analysis (PCA) were generated to enhance lithological contrast and support accurate interpretation. A point-based sampling technique was employed to extract representative training datasets, which were subsequently used in supervised lithological classification employing SVM and ANN algorithms. These classifications were driven by the enhanced remote sensing outputs derived from the image processing techniques (FCC, BR, PCA), presenting a more detailed lithological mapping of the study area compared to earlier regional assessments.

As a first study, the current research aims to develop a high-resolution geological map of the Upper Mereb area by integrating L9 multispectral data and gravity data using machine learning techniques, specifically ANN and SVM. The combination of remote sensing and gravity datasets, analyzed through advanced classification algorithms, allows for more accurate litho-structural interpretations. The novel integration of high-resolution L9 multispectral imagery and gravity data, analyzed using machine learning techniques assist to produce a detailed geological mapping in the Upper Mereb area. The developed geological map guides mineral and groundwater exploration. It improves accuracy, reduces exploration risks, and supports sustainable resource management.

2. Study area & geological background

The Study area, upper Mereb catchment, is in the southern part of Eritrea (Zoba Debub, local administrative name) and represents a geologically complex region shaped by different tectonic and sedimentary processes. It covers five administrative subzones: Galanefhi, Debarwa, Mendefera, Dekemhare, and Mai-Ayni (Fig. 1). It has a total area of 1400 km^2, where its geographic location lies in 38^0 49$^{'}$ 58$^{'}$ E and 15^0 2$^{'}$ 28″ N. The area is generally drained by a seasonal non-active river (Mereb river) running from north to south.

Geologically, the upper Mereb catchment is part of the Arabian-Nubian Shield (ANS), a significant Neoproterozoic (900–500 Ma) geological province formed by the convergence of East and West Gondwana (Ali et al., 2013; Collins and Pisarevsky, 2005; Ghebreab et al., 2009; Hamimi et al., 2022). This shield represents a complex assemblage of igneous and metamorphic rocks that evolved through accretionary processes (Solomon and Quiel, 2006; Teklay, 2006). The lithological framework of the study area is characterized by a Precambrian metamorphic basement, which is overlain by Paleozoic and Mesozoic sedimentary formations, as well as widespread Tertiary basaltic lava flows and granitoids. This complex geological history has played a crucial role in shaping the region's topography and hydrological patterns (Solomon and Ghebreab, 2006). The catchment exhibits significant lithological diversity, with metamorphic and basalt rocks constituting a major component of the geological units (Fig. 2). Schistose metavolcanic rocks, primarily composed of chlorite-epidote-quartz-muscovite schists, are prevalent, accompanied by metasedimentary formations such as slates and greywacke. Granitoid intrusions vary in composition, ranging from foliated and gneissose granite to granodiorite and diorite. The volcanic succession is dominated by alkali-olivine basalt flows, underlain by a well-developed lateritic paleosol. Additionally, the presence of Mesozoic sedimentary deposits and weathered crystalline formations further enhances the lithological complexity of the area

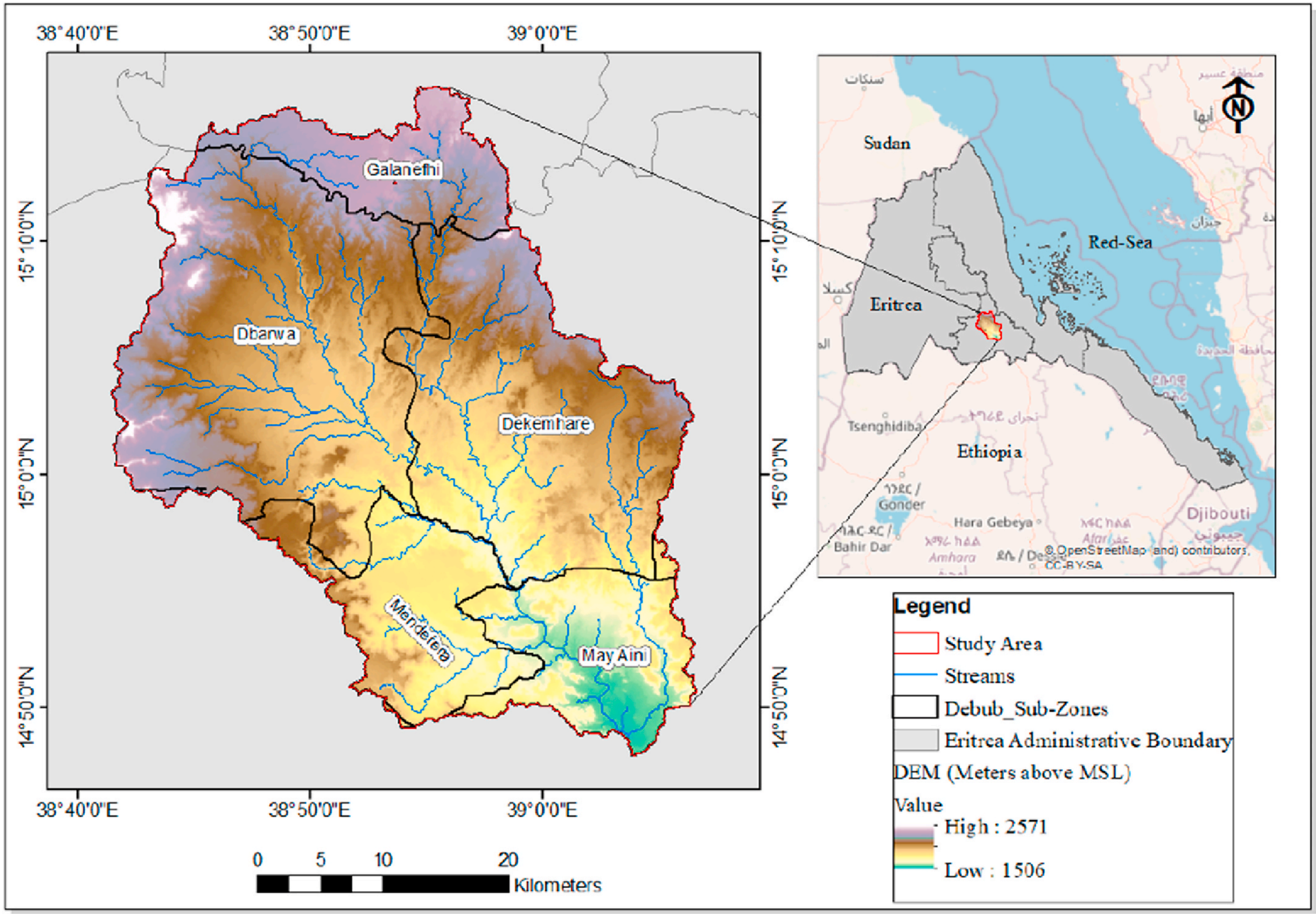

Fig. 1. Geographical location of the study area.

(Solomon and Quiel, 2006)

The tectonic framework of the Eritrean Highlands is defined by an extensive network of joint systems, fault zones, and dyke swarms, which play a significant role in shaping the region's structural and geological evolution. The research area's hydrogeological characteristics and watershed have been significantly influenced by such structures (Solomon and Ghebreab, 2006). The primary fault structures are categorized as strike-slip and normal faults, commonly exhibiting fault breccia, gouge, and well-developed slicken lines. The dominant lineament orientations NW-SE, N-S, NE-SW, and ENE-WSW reflect the strong tectonic influence of the Red Sea rift system. Sub-vertical dyke swarms, primarily composed of basaltic to dolerite intrusions, transect both granitic and basaltic formations, significantly enhancing secondary porosity and permeability (Solomon and Quiel, 2006).

3. Data & methodology

A comprehensive integration of different datasets and methodologies has been employed to achieve the main objectives of the present study. The key aspects of this approach are summarized below and illustrated in Fig. 3.

3.1. Remote sensing

L9 imagery (LC09_L1TP_169050_20220515_20230416_02_T1) was downloaded from the US geological survey (https://www.earthexplorer.usgs.gov) covering path 169 and row 50, which cover the study area with a spatial resolution of 30 m and bands covering the visible, near infrared, and shortwave infrared regions covering the study area (Table 1).

False Color Composite (FCC) images utilize various combinations of spectral bands to visualize surface features that are invisible to the naked eye. It serves as a powerful tool in remote sensing for emphasizing geological structures, mapping vegetation, and identifying mineralogical compositions with greater precision (Liu and Mason, 2013). The use of FCC allows for a rapid and cost-effective

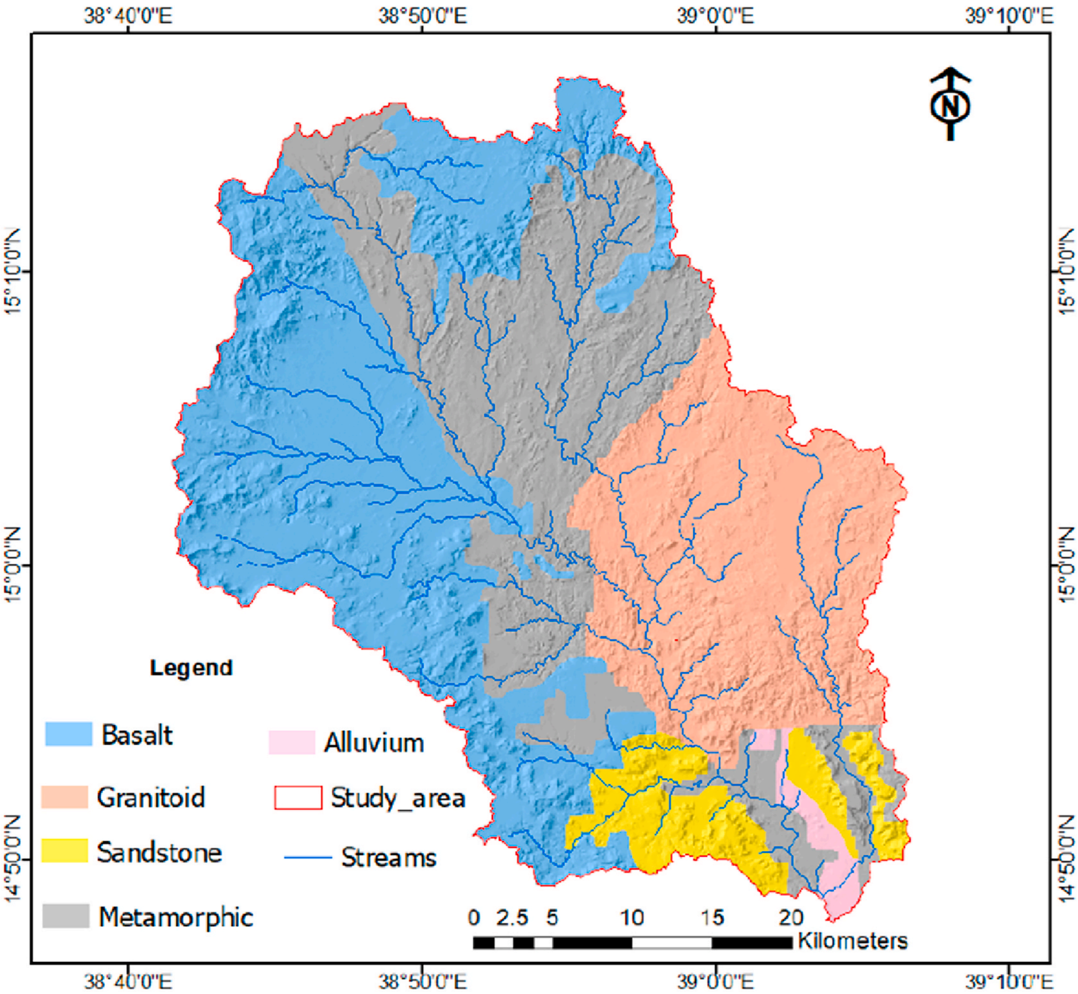

Fig. 2. Geological map of Upper Mereb area redrawn and modified after Solomon and Quiel, 2006.

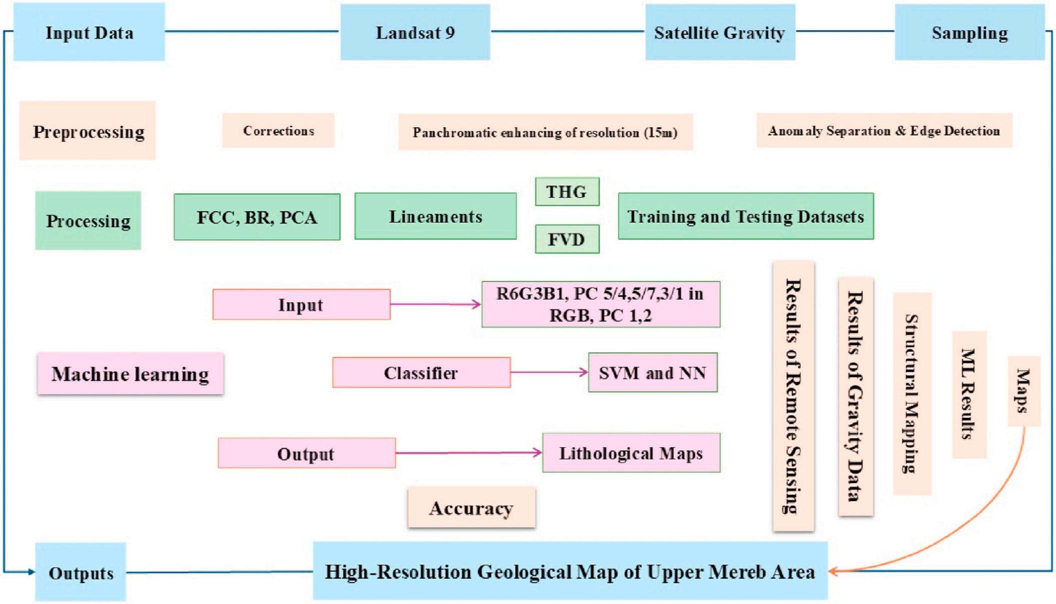

Fig. 3. Flowchart illustrates datasets and methodology used in the current study. FCC: False color composite bands; BR: Band ratio; PCA: Principal component analysis; THG: Total horizontal gradient; FVD: First vertical derivative; SVM: Support vector machine; NN: Neural network.

Table 1
Characteristics of spectral sensor (L9).

Sensor	Wavelength (μm)	Bands	Spectral Region	Spatial Resolution (m)
L9	(0.43–0.45)	B1	Coastal aerosol	30
	(0.45–0.51)	B2	Blue	
	(0.53–0.59)	B3	Green	
	(0.64–0.67)	B4	Red	
	(0.85–0.88)	B5	NIR	
	(1.57–1.65)	B6	SWIR 1	
	(2.11–2.29)	B7	SWIR 2	
	(0.50–0.68)	B8	Panchromatic	15
	(1.36–1.38)	B9	Cirrus	30
	(10.6–11.19)	B10	TIRS 1	100
	(11.50–12.51)	B11	TIRS 2	

evaluation of the discrimination lithological units in the selected study area. Band ratioing (BR) involves dividing the reflectance values of one spectral band by another, effectively enhancing subtle spectral features associated with specific minerals and surface materials (Abrams and Yamaguchi, 2019; Abrams et al., 1983; Sabins, 1999). Different BRs used to identify ferric, ferrous, carbonates, sulfates and hydroxyl-bearing minerals. PCA is a multivariate statistical technique operating under the assumption that minimal information is lost while reducing data dimensionality and highlighting key patterns and variations (Huang and Pan, 2004). In remote sensing, PCA reduces redundancy in highly correlated spectral bands and enhances features useful for interpretation and helps distinguish precise spectral differences and enhance feature-oriented band ratios to improve the discrimination of different lithological units.

3.2. Gravity

Gravity data for the study area were obtained from the GGMPlus model, which provides high-resolution gravity field data derived from satellite missions such as GRACE (Gravity Recovery and Climate Experiment) and GOCE (Gravity field and steady-state Ocean Circulation Explorer), combined with terrestrial gravity measurements, topographic data, and EGM2008 (Earth Gravitational Model, 2008). The GGMPlus dataset ensures global coverage with a spatial resolution of approximately 200 m, offering detailed gravity field variations. The extracted gravity data included free-air gravity anomalies, Bouguer gravity anomalies, and terrain corrections. Free-air anomalies were used to study variations in the Earth’s gravitational field at the geoid’s surface, while Bouguer anomalies, corrected for topographic mass contributions, provided insights into subsurface density variations (Mohieldain et al., 2025). Preprocessing steps involved filtering to reduce high-frequency noise and removing long-wavelength components to eliminate regional trends.

3.2.1. Potential field techniques

Gravity data contain the sum of the effects of different sources, including shallow and deep bodies. These two components are the regional (deep) and residual (shallow) anomalies (Eldosouky et al., 2020, 2022; Elkins, 1951; Hirt et al., 2013; Núñez-Demarco et al., 2023). The regional field represents the long-wavelength, low-frequency variations in the potential field data, while the residual anomaly highlights the shorter-wavelength, high-frequency variations. In this study, a Gaussian regional-residual filter with a standard deviation of 0.456 is applied for the anomaly separation. For creating filters to distinguish regional and residual anomaly fields, the power spectrum approach was used (Mohammed et al., 2024). Using the Fast Fourier transform (FFT) approach, spectral analysis is carried out in the wavenumber domain. FFT shifts the data from the time domain to the frequency domain aiding in the characterization and modeling of subsurface geology.

The total horizontal derivative (THD) or horizontal gradient of potential field data quantified the rate of change of the gravitational and magnetic fields strength in the horizontal direction (Camacho and Alvarez, 2021; Grauch and Cordell, 1987). It provides information about the lateral variations in the gravity and magnetic fields with the geological structures located in the highest amplitude of the resulting anomalies (THD>0). The magnitude of the horizontal gradient are calculated as a vector sum of horizontal derivatives of x (E-W) and y (N-S) for the gravity gravititional field (g) (Eq. (1)) as

$$THD = \sqrt{\left(\partial g/_{\partial x}\right)^2 + \left(\partial g/_{\partial y}\right)^2} \tag{1}$$

The first vertical derivative (FVD) of gravity data captures the rate of change in the gravitational and fields strength with respect to the vertical direction (). It provides insight into the vertical distribution of subsurface density contrasts (Keating, 1995). In the analysis of the FVD map, the areas of higher than zero anomalies represent the edge of the causative bodies. It can be obtained by Eq. (2) as

$$FVD = \sqrt{\left(\partial g/_{\partial z}\right)^2} \tag{2}$$

3.3. Field observations and sampling

A field survey was conducted in and around the upper Mereb catchment area and 38 samples were collected from five administrative subzones. The primary aim of this investigation is to prepare detailed geological data for the Upper Mereb Catchment area. The fieldwork was conducted during September 2024. Essential tools utilized during data collection included a handheld GPS device, a mobile application clinometer, a rock hammer, a field notebook, and a hand lens. Data was systematically recorded in both physical field notebooks and digital formats, including spreadsheets for precise organization and analysis. The mobile application clinometer proved invaluable for measuring structural data including the strike, dip, and orientation of rock units while simultaneously integrating coordinate information and capturing georeferenced images for future reference and improved spatial visualization. The geological structures such as faults, folds, joints, and bedding planes were observed to ensure a comparative representation of structural relationships with other methods such as DEM and gravity data. Contact types and lithological boundaries were identified through detailed field mapping and visual inspection. Geomorphological features were analyzed using topographic maps and aerial imagery, to enhance spatial accuracy and understanding of surface processes. Photographic documentation, cross-sections, and geological sketches complemented the data collection, providing a robust framework for interpretation.

3.4. Machine learning algorithms

Support Vector Machine (SVM), a widely used machine learning algorithm, has become a popular choice for lithological mapping over the past decade due to its ability to handle high-dimensional and non-linearly separable datasets. In remote sensing applications, achieving precise lithological mapping requires the optimal selection of input data. To accomplish this, advanced techniques are essential to reduce data redundancy, enhance discriminative power, and improve computational efficiency (Chen et al., 2023; Pal and Foody, 2010; Wang and Zuo, 2024).

Based on results from the L9 satellite image (FCC, BR, PC's), and the detailed field observations and sampling, the training and testing data for MLA were generated as point datasets due to complexity of lithological rock units within the selected study area (Table 2) in percentage of (20–30 % for testing data and 70–80 % for training data). The training data were generated from

Table 2
Training and testing data used to map the lithological units using machine learning models.

Lithology	Training data	Testing data	Percentage %
Basalt	875	227	25.943
Laterites	834	273	32.734
Metasediments	849	212	24.97
Metavolcanics	928	245	26.40
Granitoids	889	264	29.70
Sedimentary sequences	816	243	29.79
Water body	786	177	22.52

discriminative maps enhanced through remote sensing techniques including FCC, BR, and PCA and were further validated by extensive field observations. The classification process for the ANN and SVM were conducted using the ENVI software. For the ANN algorithm, the training process was guided by a training rate of 0.200 and a momentum value of 0.9 to enhance convergence stability. To optimize classification accuracy, the ANN logistic activation parameters were adjusted, ensuring an effective learning process. A single hidden layer was employed to balance computational efficiency with classification performance and 1000 training alterations were performed. For the SVM algorithm the Radial Basis Function (RBF) kernel (0.333) was applied, with a penalty parameter of 100. Using an RBF kernel with a gamma of 0.333 allows the SVM to acquire non-linear patterns effectively, while a penalty parameter of 100 ensures that misclassification is heavily disciplined. This combination is the result of careful hyperparameter tuning to achieve high accuracy and precise lithological mapping in such complex terrains. These specific values aim to balance the trade-offs between generalization, model complexity, and classification precision.

4. Results

4.1. Remote sensing

In recent years, Landsat OLI-8 and 9 have been effectively employed to discriminate complex lithological rock units in arid regions. The preprocessing of the imagery was performed to enhance the visualization of various bands, following standard methods for satellite image enhancement. Subsequently, different FCC were tested, and the combination 631 in RGB was identified as the most suitable for discriminating against the major lithological rock units in the study area (Fig. 4a) as an optimum index factor (OIF) of FCC. PCA and unsupervised classification were also conducted to evaluate how these algorithms can differentiate rock units.

Several band ratios were adjusted to the major mineral composition of the rocks, such as ferric iron, ferrous, and hydroxyl minerals to refine the discrimination process. Based on these analyses, we identified an FCC extracted from band ratios that successfully delineated all lithological units within the study area (Fig. 4b). Basaltic flows were identified as a major rock unit predominantly located in the western part of the study area (Fig. 4c). In the eastern region, we successfully distinguished between metavolcanic units, possibly meta-rhyolite, and metasedimentary units such as chert (Fig. 4d). Additionally, large deposits of laterite were mapped in both the northern and southern parts of the study area.

The combinations of PCA, unsupervised classification, and customized FCCs such as PC-R6G3B1, PC-R54G57B31, and R2154G56B67 recognize useful results in identifying and mapping the lithological units as shown in Figure (5). These techniques revealed lithological units within the selected study area, such as the extent of lateritic deposits. By integrating multiple images processing techniques, a proposed geological map of the study area was generated. The resolution of the imagery was enhanced to 15 m using pan sharpening with Band 8, improving the spatial detail of the analysis. Various FCCs were tested to optimize lithological discrimination, and a combination derived from band ratios specifically adjusted to the mineralogical composition of the rocks proved effective in delineating the major rock units. The accomplishment was achieved by iteratively testing FCCs and optimizing BR to enhance the separation of rock types based on their mineral compositions, leading to improved lithological mapping.

4.2. Geophysical data analysis

The complete Bouguer anomaly map (Fig. 6a) displays the spatial variation of gravity anomalies across the study area, ranging from approximately −165 mGal to −121 mGal. The map highlights significant gravity highs and lows, reflecting the combined effects of density variations from both shallow and deep subsurface structures. Gravity highs are interpreted as areas underlain by dense rock units such as mafic intrusions or compact crystalline basement rocks, while gravity lows likely correspond to less dense sedimentary cover or fractured zones. To enhance the interpretation of deeper structures and reduce the data noise, the Bouguer anomaly map was upward continued by 100 m (Fig. 6b), effectively suppressing high-frequency noise and isolating regional trends. Subsequently, the anomaly separation was conducted. The regional anomaly map (Fig. 6c) was derived to highlight deeper gravity sources and trends. This map delineates large-scale lineaments representing regional tectonic structures, which are likely associated with crustal deformation during the evolution of the Arabian-Nubian Shield. In contrast, the residual anomaly map (Fig. 6d) emphasizes shallower features by removing the regional component. This map highlights sharper and more localized lineaments, which correspond to shallow faults, fractures, or lithological boundaries near the surface.

The total horizontal derivative map (Fig. 7a) enhances lateral density variations in the gravity field, making it particularly effective in delineating edges of subsurface structures. Prominent linear features identified in this map correspond to significant fault zones and lithological boundaries. The first vertical derivative map (Fig. 7b) emphasizes near-surface features by highlighting abrupt changes in density contrast. The extracted lineaments from these derivative maps show clear patterns that align with the regional tectonic framework of the Arabian-Nubian Shield. The identified lineaments predominantly exhibit NE-SW and NW-SE orientations, which reflect the tectonic forces acting on the region. The NE-SW trending lineaments are likely associated with extensional tectonic regimes related to the opening of the Red Sea, while the NW-SE trending lineaments may be linked to strike-slip faulting or oblique tectonic stresses resulting from the interaction of the Arabian and African plates. The regional lineaments, observed in the upward-continued and regional anomaly maps, represent deep-seated crustal features that may have formed during ancient tectonic events. Conversely, the residual lineaments, identified in the residual anomaly and derivative maps, correspond to shallow structures that may influence surface processes such as groundwater flow and mineralization.

The development of the lineaments map in the study area involved the integration of multiple data processing techniques, including residual gravity anomaly, THD, regional anomaly, and FVD analysis. These techniques each highlight specific geological and structural

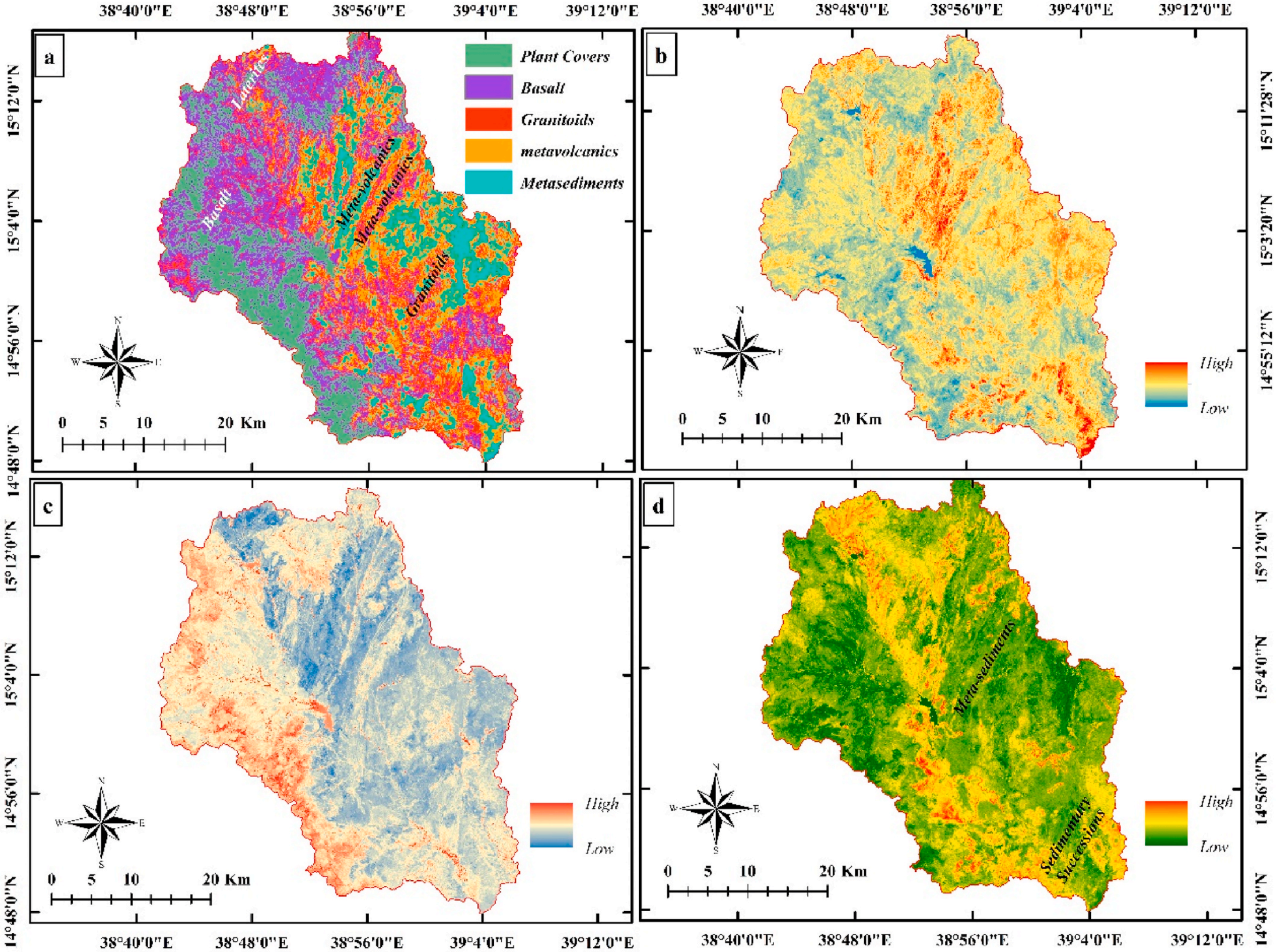

Fig. 4. (a) Maximum likelihood supervised classification; (b) ferric oxide bands 4/3; (c) bands 5/6; (d) bands 6/7.

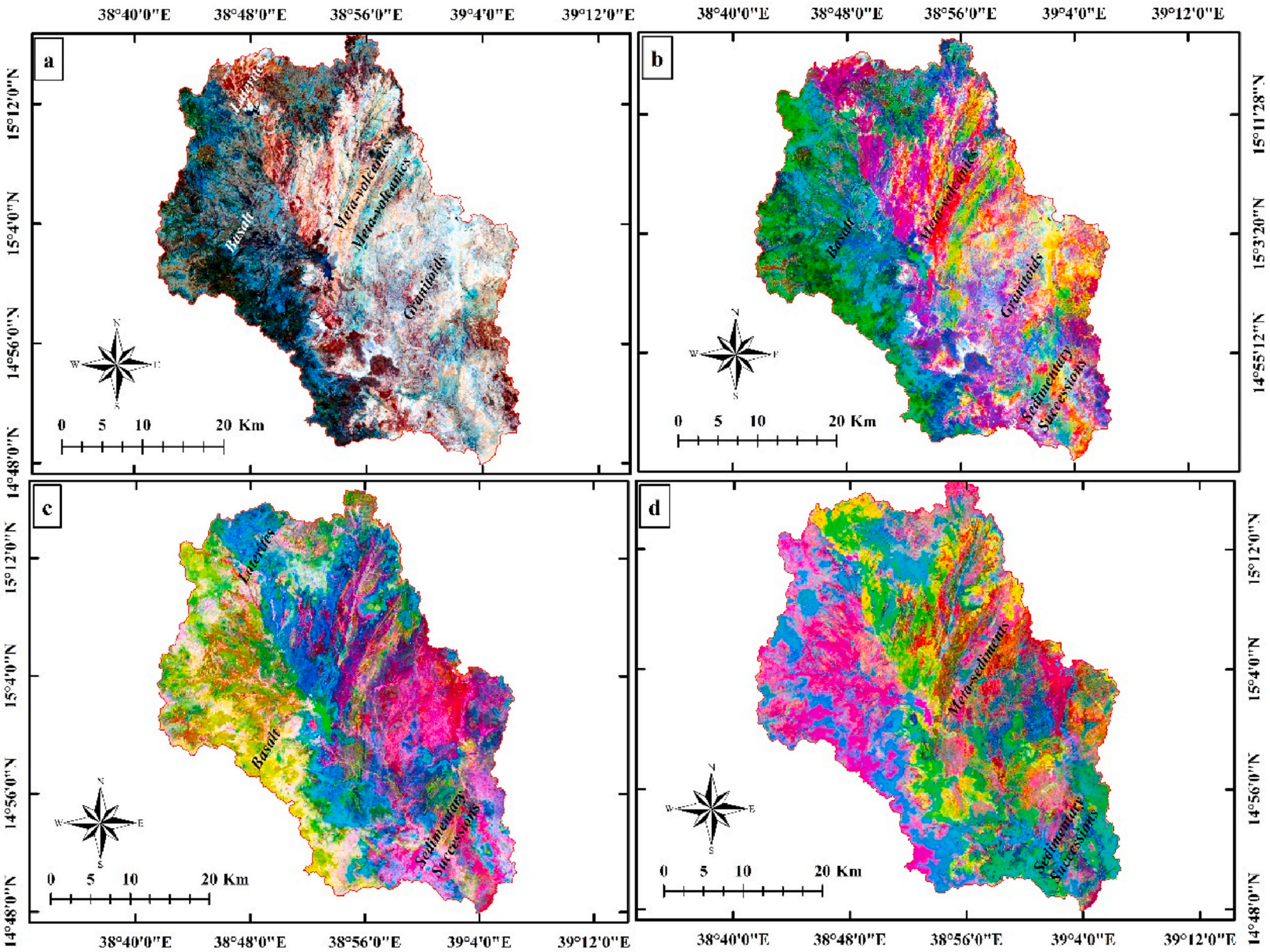

Fig. 5. Lithological discrimination of L9; (a) OIF of 631 in RGB; (b) FCC from band ratios delineate the basaltic rock units; (c) PC of bands 5/4,5/7,3/1in RGB; (d) 2/1–54, 5/6, 67 in RGB delineating lateritic deposits within the study area by different band ratios based on the special signature of laterite.

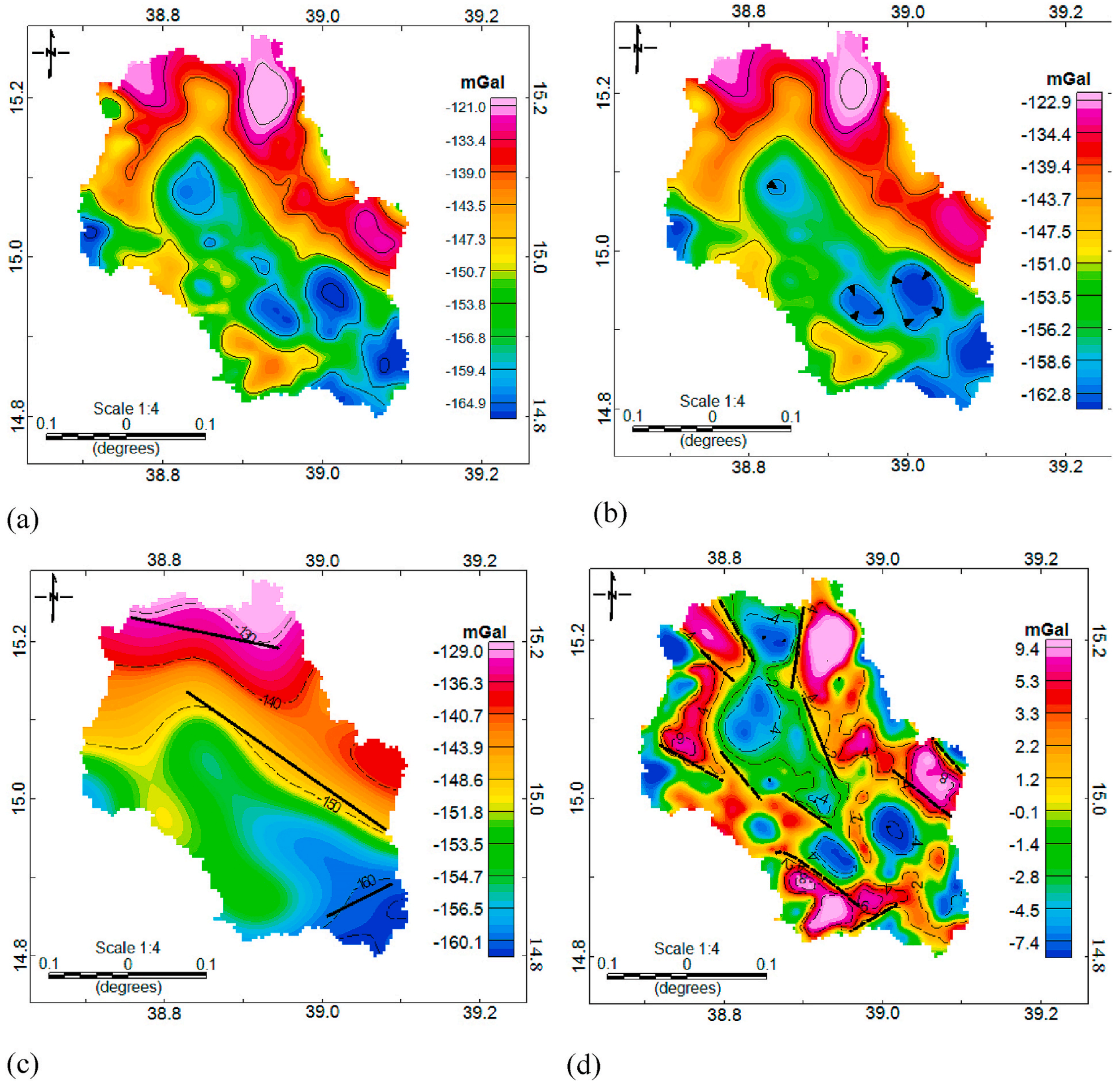

(a) (b) (c) (d)

Fig. 6. (a) Bouguer anomaly map; (b) Upward continued Bouguer anomalies to 100 m; (c) Regional anomaly map; (d) Residual anomaly map of Upper Mereb area.

features based on the nature of their sensitivity to density contrasts and spatial frequency filtering. The composite lineament map shows the distribution of lineaments obtained from these various techniques overlaid on a digital elevation model (DEM), with their respective contributions marked in distinct colors (Fig. 8). The lineaments extracted from the residual gravity anomaly primarily emphasize shallow subsurface structures while the regional anomaly delineates deeper and broader structural trends. The THD further sharpens the edges of density contrasts, providing high-resolution detail on the lateral boundaries of subsurface features. The lineaments derived from THD show good agreement with those identified in the residual anomaly map, particularly for shallow and near-surface features. FVD-derived lineaments often overlap with THD results, reinforcing the reliability of the mapped shallow structural features. Hillshade analysis, based on the digital elevation model, provides a topographic perspective and enhances the identification of surface lineaments. While the hillshade-derived lineaments align well with those from residual and derivative analyses in areas

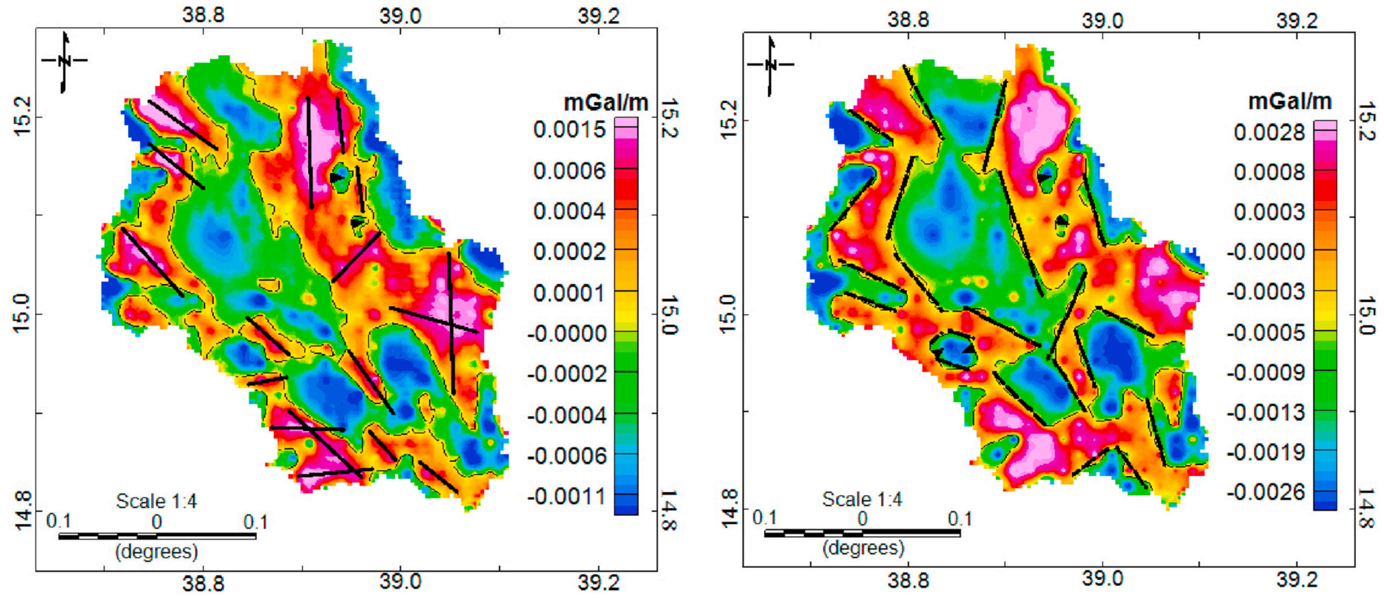

(a) (b)

Fig. 7. (a) The total horizontal derivative map showing fault zones and lithological boundaries; (b) The first vertical derivative map showing near-surface features and density contrast.

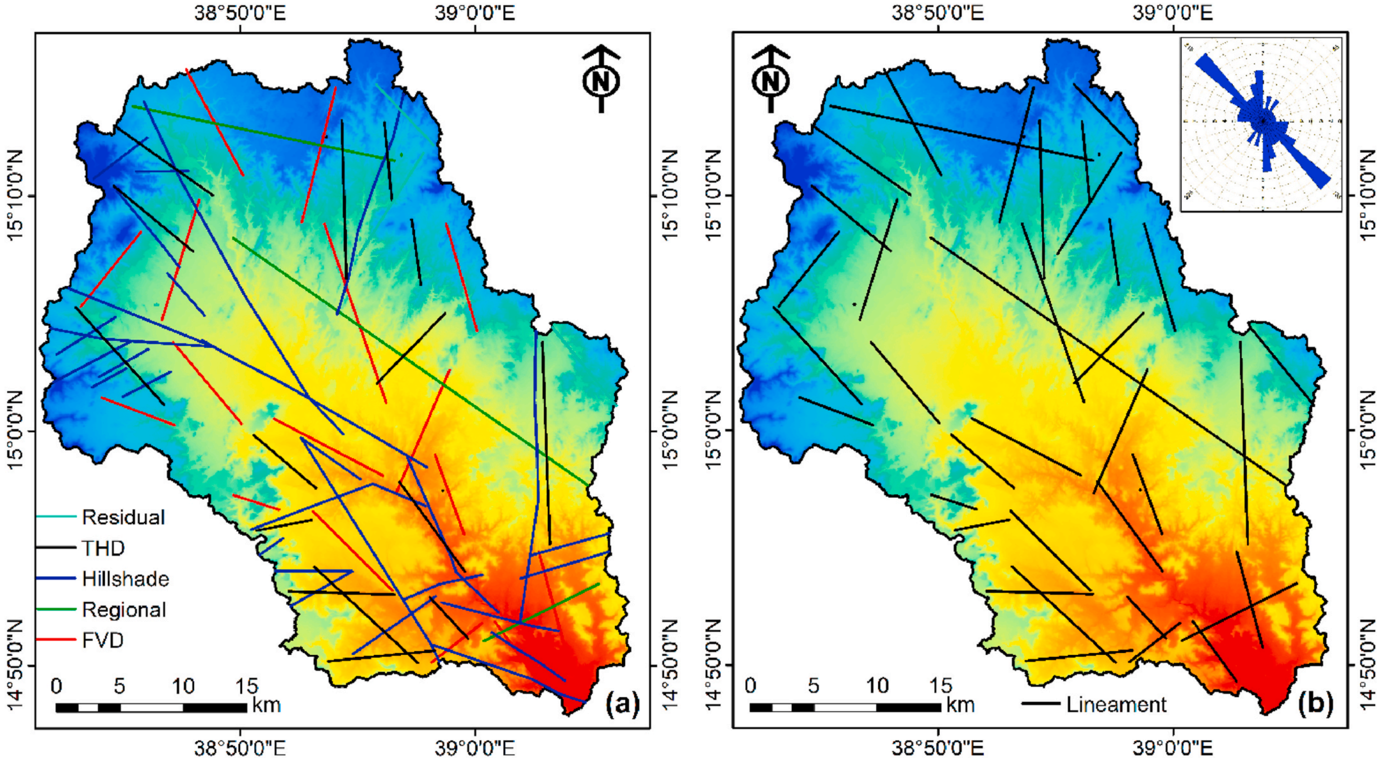

Fig. 8. Integration of lineamnets obtained from (a) gravity data, (b) hillshade from elevation model.

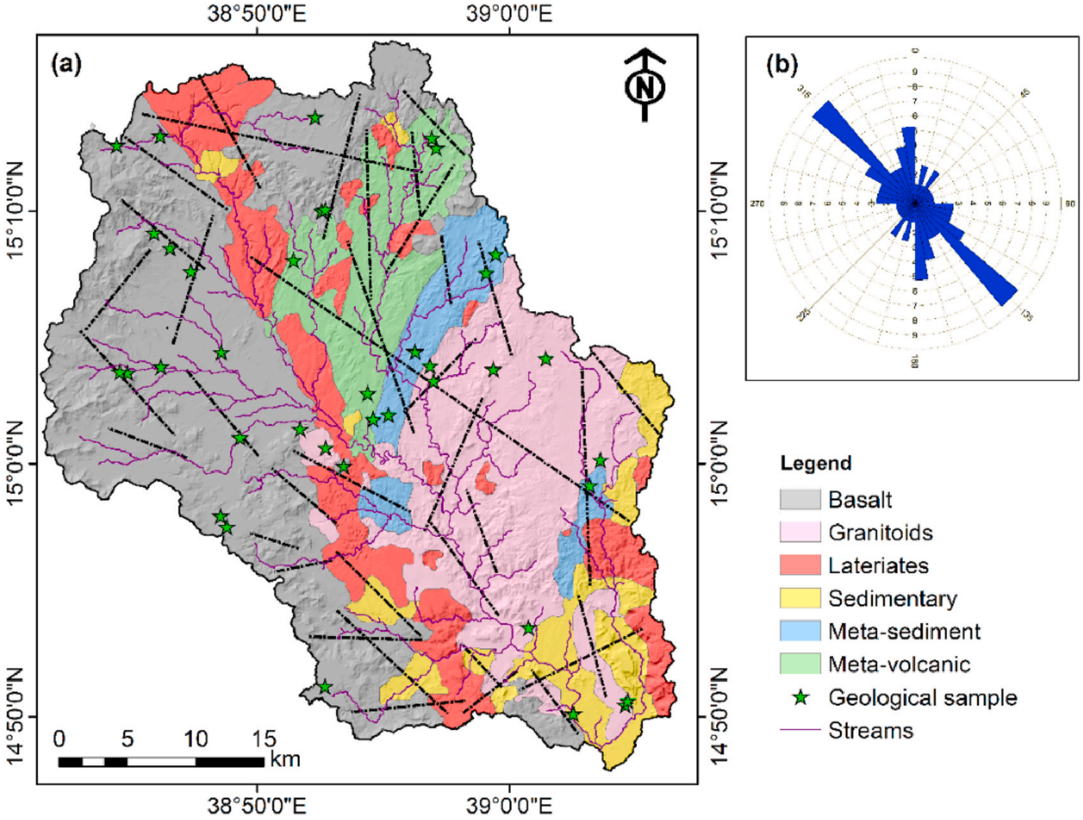

Fig. 9. Geological map of Upper Mereb obtained from the analysis of remote sensing and gravity data and validated by detailed field observations.

where subsurface features are expressed at the surface, discrepancies arise in regions where topography does not directly correspond to subsurface structures.

4.3. Lithological and structural mapping

The study area comprises four major lithological units: intermediate metavolcanic rocks, sedimentary rocks, granitic intrusions, and basaltic lava flows, with extensive lateritic deposits developed in the northern and southern parts (Fig. 9). Field observations and structural analysis, supported by gravity data, confirm that the metavolcanic rocks are predominantly felsic to intermediate in composition and locally exhibit greenschist-type assemblages, such as at Bahri Bara. These rocks are classified as low-to medium-grade metamorphic greenschist facies and are well foliated, striking 043° with a dip of 68° toward the west (dip direction 313°) (Fig. 11h). Their upper portions are lateritized, producing both red laterite and white bauxite, sometimes interlayered to form striking red-and-white banding (e.g., Station 38). The sedimentary sequence, unconformably overlying the metamorphics in the southern part of the area (Maekeno near Mai-Ayni), extends E–W and comprises arkose sandstone, mudstone with shale intercalations, and quartz-rich sandstone. Cross-bedding in these units indicates paleocurrents trending predominantly southward. Granitic intrusions, particularly around Dekemhare and Elaba, consist mainly of quartz, sodium-rich plagioclase, and K-feldspar; the Elaba granite is quartz-phyric, with exceptionally large crystals, but is weakly resistant to weathering, contributing to extensive soil cover. Basaltic lava flows dominate the western third of the study area, unconformably overlying the lateritized basement, and are composed of multiple eruptive episodes with massive lower units and amygdaloidal upper parts. The basalt, fine-to medium-grained and olivine-phyric, typically exhibits spheroidal weathering around Monguda (Fig. 11a) and columnar jointing south of Dubarwa at Sheka Wedi Bisrat (Fig. 11d). The laterite unit (Fig. 11e), up to 10 m thick, occurs between the basalt and overlying sediments; its low permeability creates spring horizons at its upper contacts. Structurally, mafic dykes trending N–S (000/90 or 180/90) crosscut almost all units and are especially prominent in Monguda, while a dense swarm of basaltic dykes striking between 210° and 300° dips steeply westward (85–90°) (Fig. 10). Quartz veins, fractures, and joints of variable orientation are also widespread. Overall, rose diagram analysis reveals a dominant NW–SE trend of deformation, with subordinate NE–SW and N–S orientations (Figs. 8 and 9, Table 3), reflecting the complex tectono-magmatic evolution that has shaped both the geomorphology and groundwater flow regimes of the region.

The structural data of the study area were analyzed and illustrated using different stereographic and rose diagram techniques. Lineament orientations interpreted from gravity data (Fig. 10a) show regional-scale structural trends that correlate well with field-based measurements (Fig. 10b). Both datasets reveal a dominant NW–SE trend with subordinate NE–SW and N–S orientations,

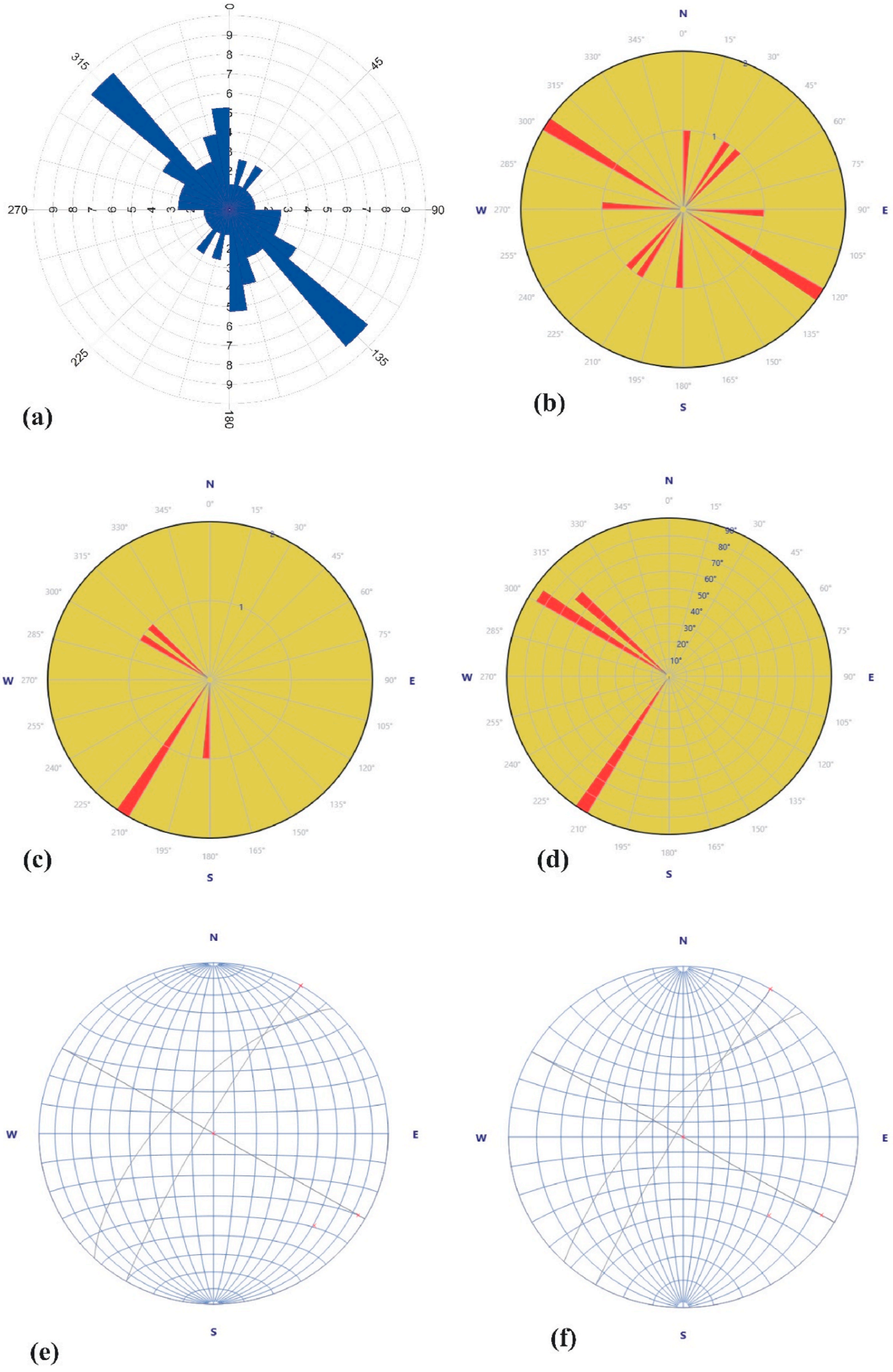

(caption on next page)

Fig. 10. Structural analysis of the Upper Mereb area: (a) rose diagram of lineaments from gravity data, (b) rose diagram of field-measured structures, (c) strike/trend distribution, (d) plunge distribution, (e) equal-area stereonet, and (f) equal-angle stereonet, illustrating dominant NW–SE trends and structural orientations.

consistent with the tectono-magmatic framework of the region. Rose diagrams representing the measured structural trends (Fig. 10c) and plunges (Fig. 10d) provide a statistical summary of directional data, highlighting the frequency distribution of foliations, joints and dykes. To visualize the orientation of planar and linear features in three dimensions, stereonet projections were employed. Equal-area projections (Fig. 10e) emphasize the true spatial distribution and density of poles to planes (see red x in Fig. 10e and f), whereas equal-angle projections (Fig. 10f) preserve angular relationships and are particularly useful for kinematic interpretations.

4.4. Machine learning algorithms

The classification results for ANN and SVM models were evaluated based on overall accuracy, kappa coefficient, confusion matrices, producer accuracy, user accuracy, and error analysis (Table 4). Fig. 12 presents the distribution of the training data for lithological prediction, showcasing its spatial and class composition. The ANN model achieved similar overall accuracy of 79.89 % to SVM (79.22 %). Similarly, the kappa coefficient for ANN (0.7648) was marginally higher than that of SVM (0.7570), indicating a comparable level of agreement between the predicted and actual classes.

The confusion matrices (Tables 5 and 6) illustrate the classification performance of both models for different lithological classes. Both models performed well in classifying Basalt, Meta-sediment, and Sedimentary units, as reflected by their high producer and user accuracy values. However, misclassification was evident in certain classes for laterites, metavolcanics, and as well as granitoids these due to complex signature and spectral similarities with adjacent lithological units of the study area and as well as within the ANS. The ANN model showed better differentiation of Meta-volcanic units than SVM but had higher commission errors, suggesting some spectral confusion with Laterites and Sedimentary rocks.

Producer accuracy for most classes was above 80 %, except for Laterites and Granitoids, which had the lowest values in both models. The ANN model provided better producer accuracy for Meta-volcanic (86.12 %) and Granitoids (68.18 %), whereas SVM had slightly higher accuracy for Sedimentary rocks. Commission and omission errors were analyzed to assess misclassification trends. Both models exhibited high commission errors for Laterites and Granitoids, suggesting spectral overlap with other rock types. While ANN performed slightly better in classifying Granitic rocks, it still showed significant errors in distinguishing Laterites and Meta-volcanic units.

The confusion matrix (Table 5) reveals several notable misclassifications that highlight underlying spectral similarities and geological interrelations among the lithological units. A considerable number of basalt samples were misclassified as granite (26 pixels), which may be attributed to overlapping spectral features, particularly in altered zones or at the margins of intrusive bodies where compositional gradients occur. Similarly, granitoids were also misclassified as basalts (26 pixels), possibly due to the presence of mafic intrusion within granitoid bodies that exhibit basalt-like spectral characteristics. The most prominent misclassification occurred between laterites and metavolcanic rocks, with 72 lateritic pixels being have a similar mineral composition and 115 metavolcanic pixels misclassified as laterites. This confusion stems from the composition relationship between these units, as laterites often develop from the intense weathering of volcanic rocks, leading to similar iron-rich, oxidized surfaces that exhibit nearly indistinguishable spectral signatures (Fig. 11e). Additionally, metamorphic units such as metasediments and metavolcanics exhibited notable confusion with sedimentary rocks. For instance, 8 pixels of metasediments and 18 of metavolcanics were classified as sedimentary rocks, due to the preservation of sedimentary rocks in low-grade metamorphosed rocks and surface weathering effects that obscure diagnostic spectral features. Granitoids also contributed to this misclassification trend, with 7 pixels confused with sedimentary rocks, possibly where granitoid surfaces are heavily weathered and fractured (Fig. 11f). These patterns emphasize the limitations of the current classification approach in distinguishing lithologies with overlapping spectral responses, particularly in transitional zones and areas affected by weathering and alteration.

The SVM classification results reveal several persistent and significant misclassifications, particularly among lithological units with similar spectral characteristics or overlapping geological contexts. One of the most prominent patterns is the confusion between metavolcanic rocks and laterites, with 110 metavolcanic pixels misclassified as laterites similarly to ANN classifier. Additionally, metasediments also exhibited notable confusion with both sedimentary rocks and granitoids; specifically, 14 metasediment pixels were misclassified as basalts, 3 as sedimentary rocks, and 9 as granitoids. These errors can be attributed to spectral overlaps caused by compositional similarities, especially in low-grade metamorphic rocks that retain sedimentary features or exhibit weathered surfaces. Basalts were largely well-classified, though a small number of pixels were confused with metasediments (8) and granitoids (8), again suggesting challenges in boundary zones or areas with altered mafic rocks. The sedimentary class showed a clear pattern of misclassification, with 41 pixels being incorrectly labeled as metavolcanics and 15 as metasediments, which may stem from insufficient spectral distinction in weathered outcrops. Granitoids, meanwhile, were misclassified as several other units, including metasediments (9), sedimentary rocks (9), and to a lesser extent, basalts (8), which may reflect spectral convergence in areas with mineralogical variation or weathering effects. These classification challenges underscore the limitations of the current spectral-based model when dealing with complex geological settings. This highlight the importance of incorporating higher-resolution datasets, such as Sentinel-2 or PRISMA, along with ground truthing to improve lithological discrimination in future mapping efforts.

The final litho-structural map of the Upper Mereb area was generated through the integration of remote sensing data, gravity measurements, and artificial neural network (ANN) algorithms, and it clearly demonstrates the delineation of lithological units with an overall accuracy of 79.89 % (Fig. 13).

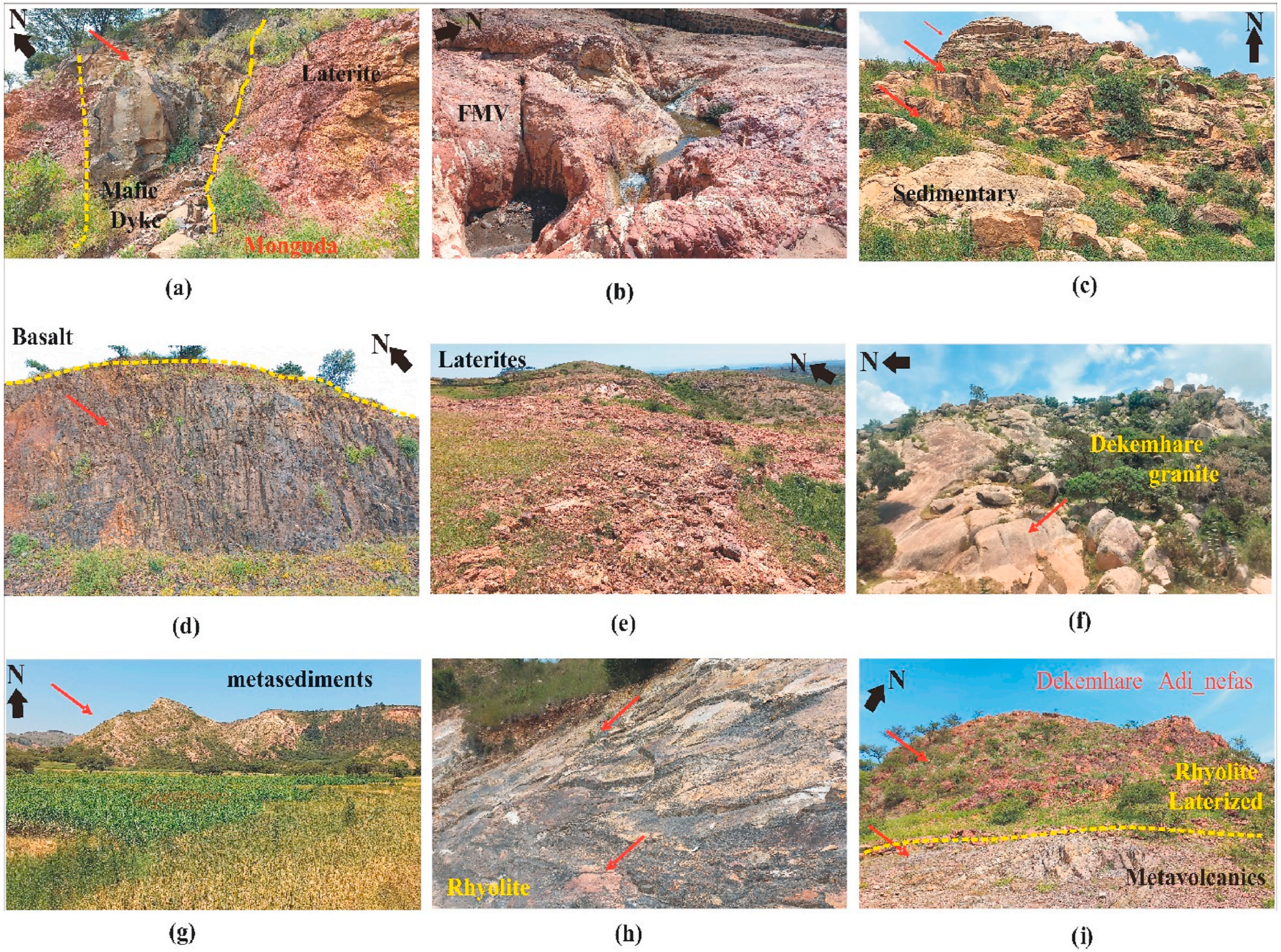

Fig. 11. Geological sample sites showing (a) Mafic dyke (Monguda area), (b) Metavolcanic (Adi-Kefelet, at Endagabir Maichelot), (c) Sedimentary rock (at Maekeno, Mai-Ayni), (d) Basalt (at sheka-wedi Bserat), (e) Laterite (near adi-zamer), (f) Granitoid (near Dekemhare), (g) Meta-sediment (near adi-keshi), (h) Rhyolite lateralized (near Gorbeati), (i) Metavolcanics with rhyolite laterite (near Dekemhare Adi_nefas).

Table 3
Structural orientation data of major lithological units in the study area.

Strike (°)	Dip (°)	Dip Direction (°)	Plunge (°)	Tag
043	68	313 (W)	–	Metavolcanic foliation
000 (or 180)	90	090 or 270	–	Mafic dykes (N–S vertical)
210	85–90	~270 (W)	–	Basaltic dyke swarm (sub-vertical, westward dip)
300	85–90	~270 (W)	–	Basaltic dyke swarm (sub-vertical, westward dip)

Table 4
Comparison of ANN and SVM classification results.

Metric	SVM Classification	ANN Classification
Overall Accuracy	79.22 % (1300/1641)	79.89 % (1311/1641)
Kappa Coefficient	0.7570	0.7648

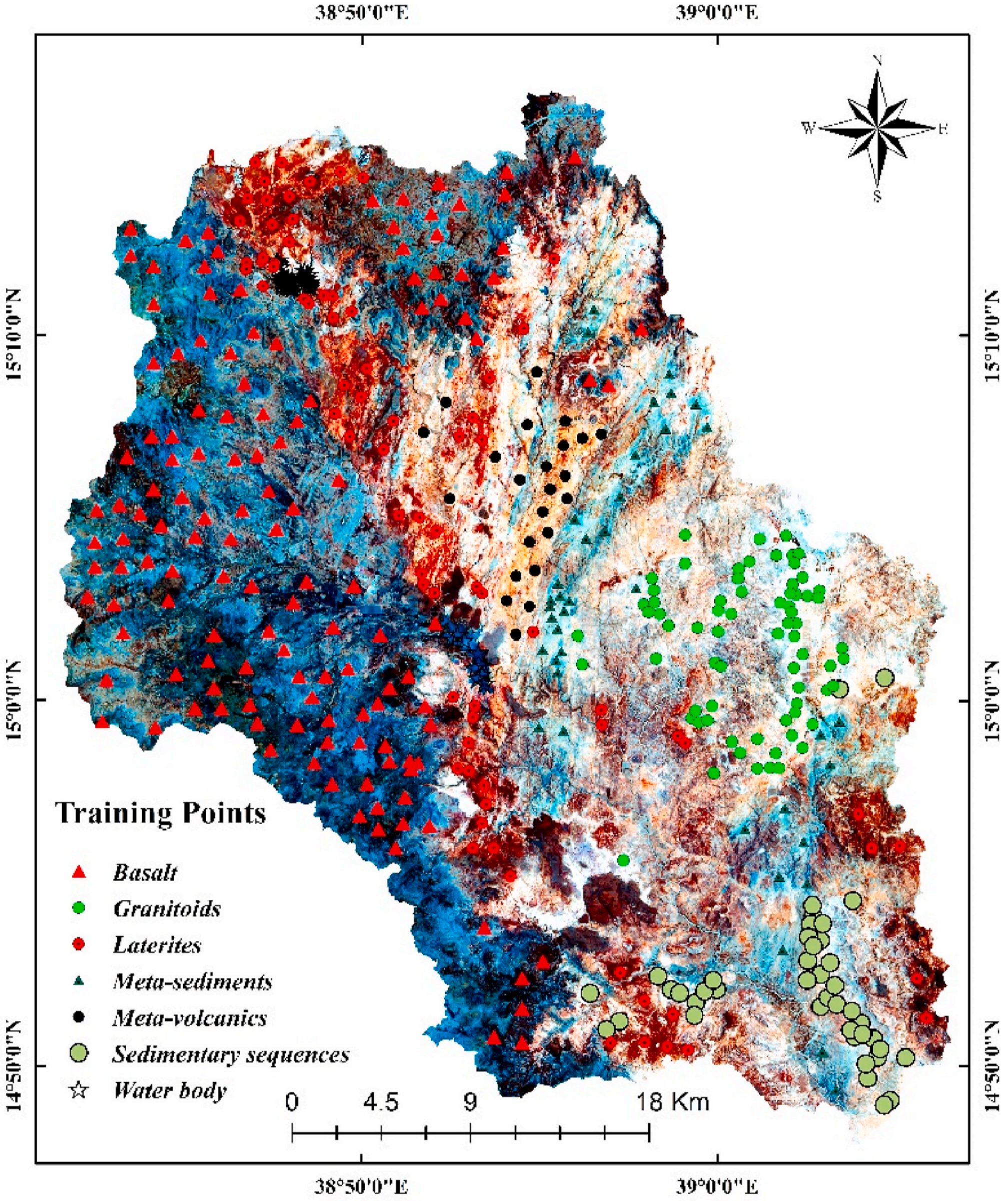

Fig. 12. The distribution of the training data used for lithological prediction.

Table 5
Confusion Matrix of ANN classifier.

Class	Basalt	Laterites	Meta-sediment	Meta-volcanic	Sedimentary	Granite	Water Body	Total
Basalt	197	0	8	3	0	**26**	0	234
Laterites	2	157	0	**72**	0	1	0	232
Meta-sediment	2	0	179	1	8	6	0	196
Meta-volcanic	0	**115**	1	211	18	5	0	350
Sedimentary	0	0	18	3	210	7	0	260
Granite	**26**	1	6	4	7	180	0	224
Water Body	0	0	0	0	0	0	177	177
Total	227	273	212	245	243	264	177	1641

Table 6
Confusion Matrix of the SVM model.

Class	Basalt	Laterites	Meta-sediment	Meta-volcanic	Sedimentary	Granite	Water Body	Total
Basalt	205	0	8	0	0	8	0	221
Laterites	0	161	0	3	0	2	0	259
Meta-sediment	14	0	178	0	3	9	0	196
Meta-volcanic	0	**110**	2	197	3	4	0	315
Sedimentary	0	0	15	**41**	228	9	0	287
Granite	8	2	9	4	9	154	0	186
Water Body	0	0	0	0	0	0	177	177
Total	227	273	212	245	243	264	177	1641

In our study area, machine learning algorithms (MLAs) demonstrated strong effectiveness in accurately delineating major lithological units, including basalts, metasediments, and granitoids. These units were generally well classified; however, some challenges developed in accurately distinguishing between sedimentary rocks and recent weathered deposits, due to their similar spectral signatures and overlapping surface characteristics. This limitation is particularly critical in zones where weathered materials overlie or are interbedded with lithologies such as basaltic flows or metamorphosed sediments, leading to potential misclassification (Bahrami et al., 2024; Ghoneim et al., 2024).

To enhance the precision of lithological mapping and to better resolve these spectral ambiguities, the use of higher-resolution multispectral and hyperspectral satellite data such as Sentinel-2 (with 10–20 m resolution) and PRISMA (with enhanced spectral sensitivity) with further algorithms (RF, XG-Boosting, CNN, and KNN) is strongly recommended. These datasets can provide better discrimination of subtle mineralogical and textural differences, thus supporting more robust classification and improving our understanding of the spatial relationships and geological transitions between basalts, metasediments, and granitoid intrusions.

5. Discussion

The application of L8 and L9 imagery, enhanced through spectral transformations and pan-sharpening techniques, demonstrated significant potential for lithological discrimination in arid environments (Abdelmalik and Abd-Allah, 2018; Hamimi et al., 2021). Among the tested FCCs, the 6-3-1 and 7-5-3 in RGB combination respectively yielded the highest spectral contrast between major rock units, supported by its OIF. This combination successfully delineated basaltic flows, metavolcanic sequences, metasedimentary rocks, and extensive lateritic covers. PCA, band ratio techniques, and unsupervised classification further improved unit separation by isolating mineral-specific spectral signatures such as ferric and ferrous iron and hydroxyl-bearing minerals. The customized FCCs (e.g., PC-R6G3B1, R2154-G56-B67) proved particularly effective in identifying lithological boundaries. These results underscore the importance of modifying spectral indices to the mineralogical characteristics of the terrain. However, despite these advances, the moderate resolution of Landsat imagery poses limitations in highly heterogeneous or weathered areas where lithologies exhibit spectral overlap or transitional zones.

Gravity data analysis, particularly the complete Bouguer anomaly map (see Fig. 6), revealed key density variations ranging from −165 mGal to −121 mGal, reflecting both shallow and deep subsurface contrasts. High gravity anomalies correspond to denser rock units such as mafic intrusions or compact basement rocks, while low anomalies mark regions with sedimentary cover or structurally weakened zones (Fig. 10). Upward continuation of the Bouguer map helped isolate regional tectonic trends, while regional-residual separation refined structural interpretation. The regional anomaly map highlighted deep-seated lineaments aligned with tectonic trends related to the Arabian-Nubian Shield (ANS), supporting crustal-scale deformation processes (Abdelsalam and Stern, 1996 Stern, 1996; Avigad and Gvirtzman, 2009; Beyth et al., 2014; Hamimi et al., 2022). Meanwhile, the residual anomaly map emphasized shallow features, including faults, joints, and lithological contacts. These structural patterns correlate well with field-observed joints, dykes, and foliations, validating the integration of geophysical and geological datasets for structural interpretation (see Fig. 11). Structurally, the study area is characterized by pervasive fracturing, jointing, and the presence of north-south trending mafic dykes. These dykes cut across all lithological units and are particularly concentrated around Monguda, reflecting late-stage magmatic activity. The synthesis of field structural data into a rose diagram revealed dominant NW–SE and subordinate NE–SW fracture orientations (Fig. 10), consistent with broader tectonic regimes of the ANS.

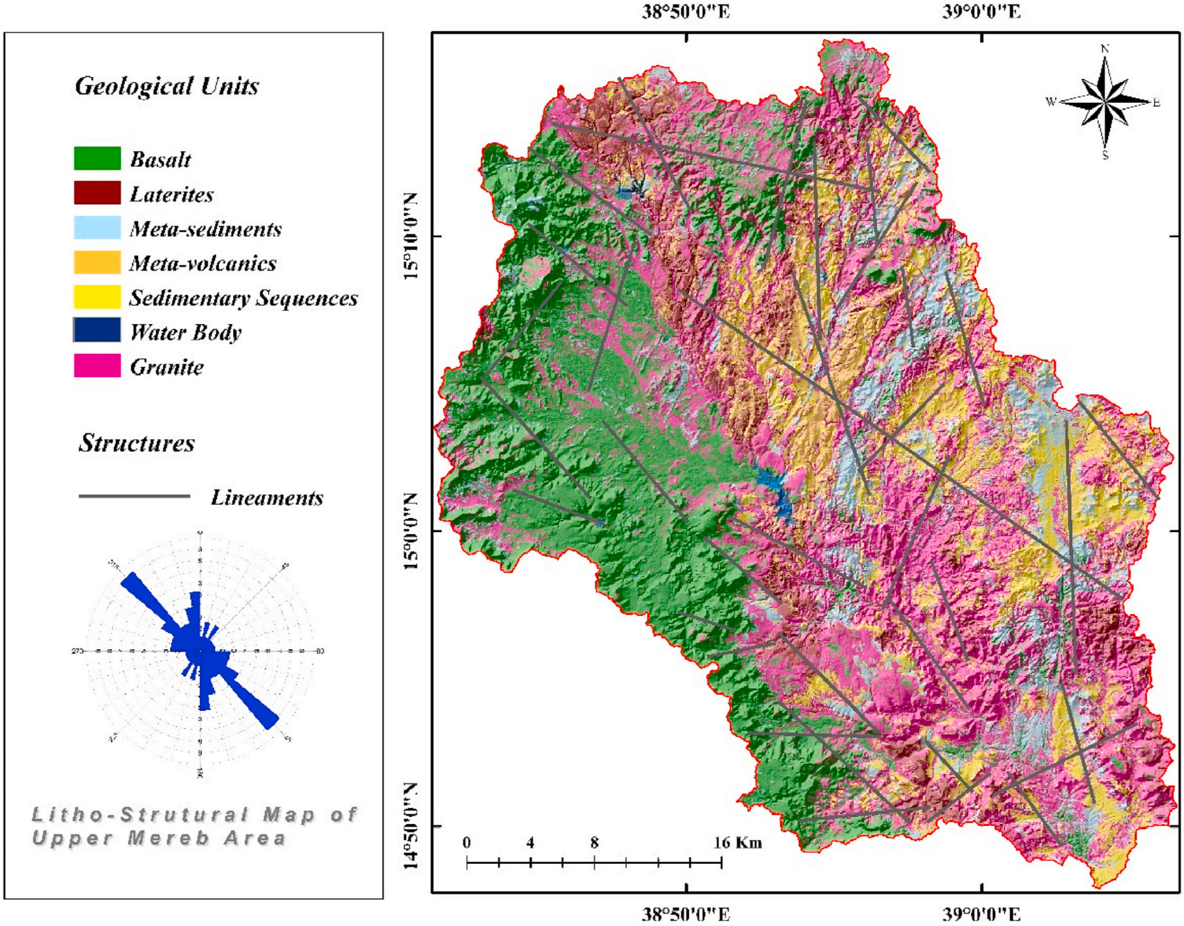

Fig. 13. Final litho-structural map of Upper Mereb area generated from integration of remote sensing, gravity data and machine learning algorithms (ANN).

The dominant NE-SW direction of the compressional forces, characteristic of the Pan-African orogeny, has played a significant role in shaping the fracture patterns (Kröner and Stern, 2004; Mohammed, 2020). The identified lineaments can be classified into three primary sets: NW-SE extension fractures, NE-SW release fractures, and N-S shear fractures. The NW-SE fractures are interpreted as extensional features formed perpendicular to the prevailing compressional stress, representing zones of crustal stretching (Abdelsalam and Stern, 1996; Shahien et al., 2021). The NE-SW fractures align with the release direction of compressional forces and likely reflect zones of stress relaxation, accommodating tectonic deformation during the Pan-African episode (Nehlig et al., 2002). Finally, the N-S trending fractures are interpreted as shear structures formed under oblique stress conditions, indicative of lateral displacement along fault planes (see Fig. 10).

Field investigations confirmed the presence of four main rock units: intermediate metavolcanic rocks, sedimentary sequences, granitic intrusions, and basaltic lava flows (see Fig. 11). The intermediate metavolcanic units, dominantly greenschist facies, display strong foliation and a consistent westward dip, likely reflecting regional tectonic compression. These rocks are of greenschist to lower amphibolite facies dominate the central region and are part of the Nakfa Terrane (Abdelsalam et al., 2000; Drury and De Souza Filho, 1998). The overlying sedimentary units, particularly the arkosic sandstone and quartz arenite, preserve sedimentary structures such as crossbedding and paleocurrent directions, pointing to a post-metamorphic depositional event.

Overall, the sedimentary rock unit is highly susceptible to both natural processes and anthropogenic activities, making it prone to weathering and erosion (Wang and Hou, 2023). Granitoid exposures, notably around Dekemhare and Elaba, exhibit quartz-phyric textures and are associated with weathered surfaces, contributing to deep soil profiles. Basaltic flows, covering the western domain, show morphological diversity from massive forms with spheroidal weathering to columnar jointing structures indicating multiple eruptive phases and cooling histories. Laterite profiles represents a significant phase of tropical weathering, which led to the leaching of soluble minerals and the enrichment of iron and aluminum oxides, giving it its characteristic red hue (Menye et al., 2025). This unit formed as a result of intense chemical weathering and rock alteration, a process that occurred during the early Paleogene period, approximately 60–50 million years ago (Banerjee et al., 2020; Westerhold et al., 2008).

MLA, specifically ANN and SVM, were employed to further enhance lithological mapping accuracy using spectral datasets. Both classifiers achieved comparable overall accuracies (ANN: 79.89 %; SVM: 79.22 %) and strong agreement with field-verified classes, particularly for basalt, sedimentary rocks, and metasediments. However, significant misclassification occurred between metavolcanic rocks, laterites, and granitoids, primarily due to overlapping spectral features. This is especially evident in the confusion between metavolcanics and laterites, a consequence of their genetic and mineralogical relationship—laterites often forming through intense weathering of volcanic rocks and exhibiting similar iron-rich reflectance. Misclassifications between granitoids and basalts, as well as between sedimentary and metasedimentary units, were likely driven by alteration effects, weathering, or compositional blending in transitional zones.

The ANN model demonstrated better sensitivity for metavolcanic and granitoid classes, while SVM showed slightly higher accuracy for sedimentary units. Nevertheless, both algorithms exhibited limitations in resolving spectrally similar or heavily weathered lithologies. The high commission and omission errors associated with laterites and metavolcanics highlight the challenges of using medium-resolution multispectral imagery for lithological discrimination in complex terrains. Given the observed classification challenges, it is evident that improving spectral resolution and data integration is crucial. Incorporating higher-resolution datasets such as Sentinel-2 (10–20 m resolution) and hyperspectral imagery from PRISMA would enhance the ability to differentiate between closely related lithological units (EL-Omairi and El Garouani, 2023; Melo and Li, 2021; Piegari et al., 2023; Zuo and Carranza, 2023). Moreover, the use of more advanced machine learning classifiers such as Random Forests (RF), XGBoost, Convolutional Neural Networks (CNN), and K-Nearest Neighbors (KNN) is recommended to handle nonlinear feature interactions and improve classification robustness. Ground-truthing, petrographic validation, and data fusion techniques (e.g., combining spectral, structural, and geophysical layers) would also contribute to refining classification outcomes and geological interpretations.

6. Conclusions

The Upper Mereb area in Eritrea represents a geologically complex region characterized by different litho-structural features that situated within the Mereb-Gash River Basin. The current study represents the first attempt to develop a high-resolution geological map of the Upper Mereb area by integrating Landsat 9 (L9) multispectral data and gravity data with machine learning techniques, specifically ANN and SVM. This integration of remote sensing and geophysical datasets enables a more accurate litho-structural interpretation, overcoming limitations associated with conventional mapping techniques.

The analysis of lineament orientations within the Upper Mereb area reveals a structural framework strongly influenced by the tectonic history of the Arabian-Nubian Shield. The dominant NE-SW direction of the compressional forces, characteristic of the Pan-African orogeny, has played a significant role in shaping the fracture patterns. The identified lineaments can be classified into three primary sets: NW-SE extension fractures, NE-SW release fractures, and N-S shear fractures. The NW-SE fractures are interpreted as extensional features formed perpendicular to the prevailing compressional stress, representing zones of crustal stretching. The NE-SW fractures align with the release direction of compressional forces and likely reflect zones of stress relaxation, accommodating tectonic deformation during the Pan-African episode. Finally, the N-S trending fractures are interpreted as shear structures formed under oblique stress conditions, indicative of lateral displacement along fault planes. The ANN model achieved an overall accuracy of 79.89 %, similarly to SVM (79.22 %), suggesting that ANN and SVM provided a marginally better agreement between predicted and actual lithological classes within the study area.

Machine learning algorithms demonstrated strong potential for lithological mapping in the study area, successfully identifying different lithological units. However, challenges remain in distinguishing between sedimentary rocks and weathered deposits due to spectral similarities. These limitations are particularly evident in transitional zones and altered rock margins. To improve classification accuracy and geological interpretation, the integration of high-resolution satellite imagery such as Sentinel-2 and PRISMA is recommended for future studies.

CRediT authorship contribution statement

Kabral Mogos Asghede: Writing – original draft, Software, Methodology, Data curation, Conceptualization. **Abazar M.A. Daoud:** Writing – original draft, Methodology, Conceptualization. **Musaab A.A. Mohammed:** Writing – original draft, Software, Methodology, Conceptualization. **Woldegabriel Genzebu:** Writing – review & editing, Data curation. **Kefela Beyene Kiflay:** Writing – original draft, Data curation. **Péter Pecsmány:** Writing – review & editing, Conceptualization. **János Vágó:** Supervision, Project administration, Conceptualization.

Declarations

The authors declare that they have no known competing financial interests or personal relationships that could have appeared to influence the work reported in this paper.

Ethical statement

The authors declare that this research was conducted in accordance with the highest ethical standards. All data used in this study were obtained from publicly available and properly cited sources, and no human or animal subjects were involved. The authors confirm that there are no conflicts of interest, and the work complies with the journal’s guidelines for ethical research and publication practices.

Declaration of competing interest

The authors declare that they have no known competing financial interests or personal relationships that could have appeared to influence the work reported in this paper.

Acknowledgment

The authors express their sincere gratitude to the Eritrean Mapping and Information Center (EMIC), the Asmara Water Resources Department and Ministry of Energy and Mines Eritrea for their support in facilitating the collection of necessary data. A special acknowledgment goes to Tedros Beyene, Senai Estifanos, Nahom Daniel, Eden Mogos, Tedros Tesfagaber, Tekle Yemane and Habteab Tsege for their support, guidance, and dedication in assisting with data collection and organization during and after the fieldwork. We express our sincere thanks to the United States Geological Survey (USGS) and the Global Gravity Model Plus (GGMplus) initiative for providing access to critical satellite imagery and geospatial datasets. The authors gratefully acknowledge the support of the University of Miskolc. Special acknowledges to the Stipendium Hungaricum Scholarship Program, established within the framework of educational cooperation between Eritrea and Hungary.

Data availability

Data will be made available on request.

References

Abdelkader, M.A., Watanabe, Y., Shebl, A., El-Dokouny, H.A., Dawoud, M., Csámer, Á., 2022. Effective delineation of rare metal-bearing granites from remote sensing data using machine learning methods: a case study from the umm Naggat area, central eastern desert, Egypt. Ore Geol. Rev. 150. https://doi.org/10.1016/j.oregeorev.2022.105184.

Abdelmalik, K.W., Abd-Allah, A.M.A., 2018. Integration of remote sensing technique and field data in geologic mapping of an ophiolitic suture zone in Western Arabian shield. J. Afr. Earth Sci. 146, 180–190. https://doi.org/10.1016/j.jafrearsci.2017.10.006.

Abdelsalam, M.G., Stern, R.J., 1996. Sutures and shear zones in the Arabian-Nubian Shield. J. Afr. Earth Sci. 23 (3), 289–310. https://doi.org/10.1016/S0899-5362(97)00003-1.

Abdelsalam, M.G., Stern, R.J., Berhane, W.G., 2000. Mapping gossans in arid regions with Landsat TM and SIR-C images: the Beddaho Alteration Zone in northern Eritrea. J. Afr. Earth Sci. 30 (4), 903–916. https://doi.org/10.1016/S0899-5362(00)00059-2.

Abrams, M.J., Brown, D., Lepley, L., Sadowski, R., 1983. Remote sensing for porphyry copper deposits in southern Arizona. Economic Geology 78 (4), 591–604. https://doi.org/10.2113/gsecongeo.78.4.591.

Abrams, M., Yamaguchi, Y., 2019. Twenty years of ASTER contributions to lithologic mapping and mineral exploration. Remote Sens. https://doi.org/10.3390/rs11111394.

Ali, K.A., Wilde, S.A., Stern, R.J., Moghazi, A.K.M., Ameen, S.M.M., 2013. Hf isotopic composition of single zircons from Neoproterozoic arc volcanics and post-collision granites, Eastern desert of Egypt: implications for crustal growth and recycling in the Arabian-Nubian Shield. Precambr. Res. 239, 42–55. https://doi.org/10.1016/j.precamres.2013.05.007.

Avigad, D., Gvirtzman, Z., 2009. Late Neoproterozoic rise and fall of the northern Arabian-Nubian shield: the role of lithospheric mantle delamination and subsequent thermal subsidence. Tectonophysics 477, 217–228. https://doi.org/10.1016/j.tecto.2009.04.018.

Bahrami, H., Esmaeili, P., Homayouni, S., Pour, A.B., Chokmani, K., Bahroudi, A., 2024. Machine learning-based lithological mapping from ASTER remote-sensing imagery. Minerals 14, 202. https://doi.org/10.3390/min14020202.

Banerjee, S., Choudhury, T.R., Saraswati, P.K., Khanolkar, S., 2020. The formation of authigenic deposits during Paleogene warm climatic intervals: a review. J. Palaeogeogr. https://doi.org/10.1186/s42501-020-00076-8.

Beyth, M., Eyal, Y., Garfunkel, Z., 2014. The geology of the northern tip of the arabian-nubian shield. J. Afr. Earth Sci. 99, 332–341. https://doi.org/10.1016/j.jafrearsci.2014.03.028.

Camacho, M., Alvarez, R., 2021. Geophysical modeling with satellite gravity data: Eigen-6C4 vs. GGM plus. Engineering 13, 690–706. https://doi.org/10.4236/eng.2021.1312050.

Chen, Y., Dong, Y., Wang, Y., Zhang, F., Liu, G., Sun, P., 2023. Machine learning algorithms for lithological mapping using Sentinel-2 and SRTM DEM in highly vegetated areas. Front Ecol Evol 11. https://doi.org/10.3389/fevo.2023.1250971.

Collins, A.S., Pisarevsky, S.A., 2005. Amalgamating eastern Gondwana: the evolution of the Circum-Indian Orogens. Earth Sci. Rev. 71, 229–270. https://doi.org/10.1016/j.earscirev.2005.02.004.

Daoud, A.M.A., Shebl, A., Abdelkader, M.M., Mohieldain, A.A., Csámer, Á., Satti, A.M.N., Rózsa, P., 2025. Remote sensing and gravity investigations for barite detection in Neoproterozoic rocks in the Ariab area, Red Sea hills, Sudan. Remote Sens. Appl. 37. https://doi.org/10.1016/j.rsase.2024.101416.

Davies, R.S., Trott, M., Georgi, J., Farrar, A., 2025. Artificial intelligence and machine learning to enhance critical mineral deposit discovery. Geosystems and Geoenvironment 4, 100361. https://doi.org/10.1016/j.geogeo.2025.100361.

Drury, S.A., Berhe, S.M., 1993. Accretion tectonics in northern Eritrea revealed by remotely sensed imagery. Geol. Mag. 130, 177–190. https://doi.org/10.1017/S0016756800009845.

Drury, S.A., De Souza Filho, C.R., 1998. Neoproterozoic terrane assemblages in Eritrea: review and prospects. Journal of African Earth Sciences 27 (3–4), 331–348. https://doi.org/10.1016/S0899-5362(98)00066-9.

Drury, S.A., De Souza Filho, C.R., 1998. Neoproterozoic terrane assemblages in Eritrea: review and prospects. J. Afr. Earth Sci. 27, 331–348. https://doi.org/10.1016/S0899-5362(98)00066-9.

Drury, S.A., Peart, R.J., Andrews Deller, M.E., 2001. Hydrogeological potential of major fractures in Eritrea. J. Afr. Earth Sci. 32, 163–177. https://doi.org/10.1016/S0899-5362(01)90002-8.

Eldosouky, A.M., Elkhateeb, S.O., Ali, A., Kharbish, S., 2020. Enhancing linear features in aeromagnetic data using directional horizontal gradient at Wadi Haimur area, South Eastern desert, Egypt. Carpathian Journal of Earth and Environmental Sciences 15, 323–326. https://doi.org/10.26471/cjees/2020/015/132.

Eldosouky, A.M., Pham, L.T., Duong, V.-H., Kemgang Ghomsi, F.E., Henaish, A., 2022. Structural interpretation of potential field data using the enhancement techniques: a case study. Geocarto Int. 37, 16900–16925. https://doi.org/10.1080/10106049.2022.2120548.

Elkins, T.A., 1951. The second derivative method of gravity interpretation. Geophysics 16 (1), 29–50. https://doi.org/10.1190/1.1437648.

El-Omairi, M.A., El Garouani, A., 2023. A review on advancements in lithological mapping utilizing machine learning algorithms and remote sensing data. Heliyon, e20168. https://doi.org/10.1016/j.heliyon.2023.e20168.

El-Omairi, M.A., El Garouani, M., El Garouani, A., 2025. Enhanced lithological mapping via remote sensing: employing SVM, random trees, ANN, with MNF and PCA transformations. The Egyptian Journal of Remote Sensing and Space Sciences 28, 34–52. https://doi.org/10.1016/j.ejrs.2024.12.001.

Ghebreab, W., Greiling, R.O., Solomon, S., 2009. Structural setting of Neoproterozoic mineralization, Asmara district, Eritrea. J. Afr. Earth Sci. 55, 219–235. https://doi.org/10.1016/j.jafrearsci.2009.05.001.

Ghoneim, S.M., Hamimi, Z., Abdelrahman, K., Khalifa, M.A., Shabban, M., Abdelmaksoud, A.S., 2024. Machine learning and remote sensing-based lithological mapping of the Duwi Shear-belt area, central eastern desert, Egypt. Sci. Rep. 14, 17010. https://doi.org/10.1038/s41598-024-66199-3.

Grauch, V.J.S., Cordell, L., 1987. Limitations of determining density or magnetic boundaries from the horizontal gradient of gravity or pseudogravity data. Geophysics 52 (1), 118–121. https://doi.org/10.1190/1.1442236.

Hamimi, Z., Abdelkareem, M., Fowler, A.-R., Younis, M.H., Matsah, M., Abdalla, F., 2021. Remote sensing and structural studies of the central Asir shear zone, Western Arabian shield: implications for the late Neoproterozoic E-W Gondwana assembly. J. Asian Earth Sci. 215, 104782. https://doi.org/10.1016/j.jseaes.2021.104782.

Hamimi, Z., Hagag, W., Fritz, H., Baggazi, H., Kamh, S., 2022. The tectonic map and structural provinces of the late Neoproterozoic Egyptian Nubian shield: implications for crustal growth of the arabian–nubian shield (East African orogen). Front. Earth Sci. 10. https://doi.org/10.3389/feart.2022.921521.

Harris, J.R., Grunsky, E.C., 2015. Predictive lithological mapping of Canada's North using random forest classification applied to geophysical and geochemical data. Comput. Geosci. 80, 9–25. https://doi.org/10.1016/j.cageo.2015.03.013.

Hirt, C., Claessens, S., Fecher, T., Kuhn, M., Pail, R., Rexer, M., 2013. New ultrahigh-resolution picture of Earth's gravity field. Geophys. Res. Lett. 40, 4279–4283. https://doi.org/10.1002/grl.50838.

Huang, B., Pan, B., 2004. Characteristics of log responses and lithology determination of igneous rock reservoirs. J. Geophys. Eng. 1, 51–55. https://doi.org/10.1088/1742-2132/1/1/006.

Johnson, P.R., Halverson, G.P., Kusky, T.M., Stern, R.J., Pease, V., 2013. Volcanosedimentary basins in the arabian-nubian shield: markers of repeated exhumation and denudation in a neoproterozoic accretionary Orogen. Geosciences. https://doi.org/10.3390/geosciences3030389.

Kassa, M., 2024. Investigating subsurface structural lineaments of the northwest Ethiopian plateau using gravity data. Heliyon 10, e35520. https://doi.org/10.1016/j.heliyon.2024.e35520.

Keating, P., 1995. A simple technique to identify magnetic anomalies due to kimberlite pipes. Explor. Min. Geol. 4, 121–125.

Kröner, A., Stern, R.J., 2004. Africa: Pan-African orogeny. In: Encyclopedia of Geology. Elsevier Inc., pp. 1–12. https://doi.org/10.1016/B0-12-369396-9/00431-7

Liu, J.G., Mason, P.J., 2013. Essential image processing and GIS for remote sensing. John Wiley & Sons. https://doi.org/10.1002/9781118687963.

Mahboob, M.A., Celik, T., Genc, B., 2024. Predictive modelling of mineral prospectivity using satellite remote sensing and machine learning algorithms. Remote Sens. Appl. 36, 101316. https://doi.org/10.1016/j.rsase.2024.101316.

Measho, S., Chen, B., Pellikka, P., Trisurat, Y., Guo, L., Sun, S., Zhang, H., 2020. Land use/land cover changes and associated impacts on water yield availability and variations in the mereb-gash river basin in The Horn of Africa. J Geophys Res Biogeosci 125. https://doi.org/10.1029/2020JG005632.

Melo, A., Li, Y., 2021. Geology differentiation by applying unsupervised machine learning to multiple independent geophysical inversions. Geophys. J. Int. 227, 2058–2078. https://doi.org/10.1093/gji/ggab316.

Menye, A.J., Mbessa, M., Ngami, P.F., Bilong, P., 2025. Influence of garnet and micas proportions in metamorphic rocks on laterite formation and variation in their road compaction parameters. Heliyon 11, e42301. https://doi.org/10.1016/j.heliyon.2025.e42301.

Miller, D.M., Kaminsky, E.J., Rana, S., 1995. Neural network classification of remote-sensing data. Comput. Geosci. 21, 377–386. https://doi.org/10.1016/0098-3004(94)00082-6.

Mohammed, M.A.A., 2020. The use of Landsat ETM+ in hydrogeological investigation in basement terrain, Hamissana area, N-E Sudan. Humanitarian and Natural Sciences Journal 1, 370–378. https://doi.org/10.53796/hnsj1625.

Mohammed, M.A.A., Szabó, N.P., Szűcs, P., 2024. Joint interpretation and modeling of potential field data for mapping groundwater potential zones around Debrecen. Acta Geodaetica et Geophysica. https://doi.org/10.1007/s40328-023-00433-8.

Mohieldain, A.A., Dobróka, M., Mohammed, M.A.A., Szabó, N.P., 2025. Gravity-based structural and tectonic characterization of the Shendi-Atbara Basin, central Sudan. J. Afr. Earth Sci., 105571

Nehlig, P., Genna, A., Asfirane, F., BRGM, France, Guerrot, C., Eberlé, J.M., Kluyver, H.M., Lasserre, J.L., Le Goff, E., Nicol, N. and BRGM, France, 2002. A review of the Pan-African evolution of the Arabian Shield. *GeoArabia*, *7*(1), 103-124. doi:10.2113/geoarabia0701103.

Núñez-Demarco, P., Bonilla, A., Sánchez-Bettucci, L., Prezzi, C., 2023. Potential-field filters for gravity and magnetic interpretation: a review. Surv. Geophys. https://doi.org/10.1007/s10712-022-09752-x.

Pal, M., Foody, G.M., 2010. Feature selection for classification of hyperspectral data by SVM. IEEE Trans. Geosci. Rem. Sens. 48, 2297–2307. https://doi.org/10.1109/TGRS.2009.2039484.

Piegari, E., De Donno, G., Melegari, D., Paoletti, V., 2023. A machine learning-based approach for mapping leachate contamination using geoelectrical methods. Waste Manag. 157, 121–129. https://doi.org/10.1016/j.wasman.2022.12.015.

Pradhan, B., Jena, R., Talukdar, D., Mohanty, M., Sahu, B.K., Raul, A.K., Abdul Maulud, K.N., 2022. A new method to evaluate gold mineralisation-potential mapping using deep learning and an explainable artificial intelligence (XAI) model. Remote Sens. 14, 4486. https://doi.org/10.3390/rs14184486.

Pratama, I.P.D., Osawa, T., As-Syakur, A.R., 2023. Identification of fault zone in Bali using GGMPlus gravity and Alos-2 Palsar-2 data. JURNAL GEOGRAFI 15, 46. https://doi.org/10.24114/jg.v15i1.40772.

Sabins, F.F., 1999. Remote sensing for mineral exploration. Ore geology reviews 14 (3–4), 157–183. https://doi.org/10.1016/S0169-1368(99)00007-4.

Shahien, M.G., Azer, M.K., Asimow, P.D., 2021. Neoproterozoic Ophiolites of the Arabian-Nubian Shield, pp. 297–330. https://doi.org/10.1007/978-3-030-72995-0_12.

Solomon, S., Ghebreab, W., 2006. Lineament characterization and their tectonic significance using landsat TM data and field studies in the central highlands of Eritrea. J. Afr. Earth Sci. 46, 371–378. https://doi.org/10.1016/j.jafrearsci.2006.06.007.

Solomon, S., Quiel, F., 2006. Groundwater study using remote sensing and geographic information systems (GIS) in the central highlands of Eritrea. Hydrogeol. J. 14, 729–741. https://doi.org/10.1007/s10040-005-0477-y.

Stern, R.J., Johnson, P.R., Kröner, A., Yibas, B., 2004. Neoproterozoic ophiolites of the arabian-nubian shield. Developments in Precambrian Geology. https://doi.org/10.1016/S0166-2635(04)13003-X.

Teklay, M., 2006. Neoproterozoic arc-back-arc system analog to modern arc-back-arc systems: evidence from tholeiite-boninite association, serpentinite mudflows and across-arc geochemical trends in Eritrea, southern Arabian-Nubian shield. Precambr. Res. 145, 81–92. https://doi.org/10.1016/j.precamres.2005.11.015.

Wang, L., Hou, D., 2023. Plastistone: an emerging type of sedimentary rock. Earth Sci. Rev. https://doi.org/10.1016/j.earscirev.2023.104620.

Wang, Z., Zuo, R., 2024. An evaluation of convolutional neural networks for lithological mapping based on hyperspectral images. IEEE J. Sel. Top. Appl. Earth Obs. Rem. Sens. 17, 6414–6425. https://doi.org/10.1109/JSTARS.2024.3372138.

Westerhold, T., Röhl, U., Raffi, I., Fornaciari, E., Monechi, S., Reale, V., Bowles, J., Evans, H.F., 2008. Astronomical calibration of the Paleocene time. Palaeogeogr. Palaeoclimatol. Palaeoecol. 257, 377–403. https://doi.org/10.1016/j.palaeo.2007.09.016.

Zuo, R., Carranza, E.J.M., 2023. Machine learning-based mapping for mineral exploration. Math. Geosci. 55, 891–895. https://doi.org/10.1007/s11004-023-10097-3.